**Astronomy**
**&**
**Astrophysics**

# *Planck* intermediate results

## IV. The *XMM-Newton* validation programme for new *Planck* galaxy clusters

Planck Collaboration: P. A. R. Ade[85], N. Aghanim[59], M. Arnaud[74], M. Ashdown[71,6], J. Aumont[59], C. Baccigalupi[83], A. Balbi[35], A. J. Banday[91,9], R. B. Barreiro[67], J. G. Bartlett[1,69], E. Battaner[93], K. Benabed[60,89], A. Benoît[57], J.-P. Bernard[9], M. Bersanelli[32,50], I. Bikmaev[19,3], H. Böhringer[79], A. Bonaldi[70], J. R. Bond[8], S. Borgani[33,47], J. Borrill[14,87], F. R. Bouchet[60,89], M. L. Brown[70], C. Burigana[49,34], R. C. Butler[49], P. Cabella[36], P. Carvalho[6], A. Catalano[75,73], L. Cayón[29], A. Chamballu[55], R.-R. Chary[56], L.-Y. Chiang[63], G. Chon[79], P. R. Christensen[80,37], D. L. Clements[55], S. Colafrancesco[46], S. Colombi[60,89], A. Coulais[73], B. P. Crill[69,81], F. Cuttaia[49], A. Da Silva[12], H. Dahle[65,11], R. J. Davis[70], P. de Bernardis[31], G. de Gasperis[35], G. de Zotti[45,83], J. Delabrouille[1], J. Démoclès[74,⋆], F.-X. Désert[53], J. M. Diego[67], K. Dolag[92,78], H. Dole[59,58], S. Donzelli[50], O. Doré[69,10], M. Douspis[59], X. Dupac[41], T. A. Enßlin[78], H. K. Eriksen[65], F. Finelli[49], I. Flores-Cacho[9,91], O. Forni[91,9], M. Frailis[47], E. Franceschi[49], M. Frommert[17], S. Galeotta[47], K. Ganga[1], R. T. Génova-Santos[66], Y. Giraud-Héraud[1], J. González-Nuevo[67,83], R. González-Riestra[40], K. M. Górski[69,95], A. Gregorio[33,47], A. Gruppuso[49], F. K. Hansen[65], D. Harrison[64,71], A. Hempel[66,38], S. Henrot-Versillé[72], C. Hernández-Monteagudo[13,78], D. Herranz[67], S. R. Hildebrandt[10], E. Hivon[60,89], M. Hobson[6], W. A. Holmes[69], A. Hornstrup[16], W. Hovest[78], K. M. Huffenberger[94], G. Hurier[75], A. H. Jaffe[55], T. Jagemann[41], W. C. Jones[24], M. Juvela[23], R. Kneissl[39,7], J. Knoche[78], L. Knox[26], M. Kunz[17,59], H. Kurki-Suonio[23,44], G. Lagache[59], J.-M. Lamarre[73], A. Lasenby[6,71], C. R. Lawrence[69], M. Le Jeune[1], S. Leach[83], R. Leonardi[41], A. Liddle[22], P. B. Lilje[65,11], M. Linden-Vørnle[16], M. López-Caniego[67], G. Luzzi[72], J. F. Macías-Pérez[75], D. Maino[32,50], N. Mandolesi[49,5], R. Mann[84], M. Maris[47], F. Marleau[62], D. J. Marshall[91,9], E. Martínez-González[67], S. Masi[31], M. Massardi[48], S. Matarrese[30], P. Mazzotta[35], S. Mei[43,90,10], P. R. Meinhold[27], A. Melchiorri[31,51], J.-B. Melin[15], L. Mendes[41], A. Mennella[32,50], S. Mitra[54,69], M.-A. Miville-Deschênes[59,8], A. Moneti[60], G. Morgante[49], D. Mortlock[55], D. Munshi[85], P. Naselsky[80,37], F. Nati[31], P. Natoli[34,4,49], H. U. Nørgaard-Nielsen[16], F. Noviello[70], S. Osborne[88], F. Pajot[59], D. Paoletti[49], O. Perdereau[72], F. Perrotta[83], F. Piacentini[31], M. Piat[1], E. Pierpaoli[21], R. Piffaretti[74,15], S. Plaszczynski[72], P. Platania[68], E. Pointecouteau[91,9], G. Polenta[4,46], L. Popa[61], T. Poutanen[44,23,2], G. W. Pratt[74], S. Prunet[60,89], J.-L. Puget[59], M. Reinecke[78], M. Remazeilles[59,1], C. Renault[75], S. Ricciardi[49], G. Rocha[69,10], C. Rosset[1], M. Rossetti[32,50], J. A. Rubiño-Martín[66,38], B. Rusholme[56], M. Sandri[49], G. Savini[82], D. Scott[20], G. F. Smoot[25,77,1], A. Stanford[26], F. Stivoli[52], R. Sudiwala[85], R. Sunyaev[78,86], D. Sutton[64,71], A.-S. Suur-Uski[23,44], J.-F. Sygnet[60], J. A. Tauber[42], L. Terenzi[49], L. Toffolatti[18,67], M. Tomasi[50], M. Tristram[72], L. Valenziano[49], B. Van Tent[76], P. Vielva[67], F. Villa[49], N. Vittorio[35], L. A. Wade[69], B. D. Wandelt[60,89,28], N. Welikala[59], J. Weller[92], S. D. M. White[78], D. Yvon[15], A. Zacchei[47], and A. Zonca[27]

*(Affiliations can be found after the references)*

**ABSTRACT**

We present the final results from the *XMM-Newton* validation follow-up of new *Planck* galaxy cluster candidates. We observed 15 new candidates, detected with signal-to-noise ratios between 4.0 and 6.1 in the 15.5-month nominal *Planck* survey. The candidates were selected using ancillary data flags derived from the ROSAT All Sky Survey (RASS) and Digitized Sky Survey all-sky maps, with the aim of pushing into the low SZ flux, high-$z$ regime and testing RASS flags as indicators of candidate reliability. Fourteen new clusters were detected by *XMM-Newton*, ten single clusters and two double systems. Redshifts from X-ray spectroscopy lie in the range 0.2 to 0.9, with six clusters at $z > 0.5$. Estimated masses ($M_{500}$) range from $2.5 \times 10^{14}$ to $8 \times 10^{14}$ $M_\odot$. We discuss our results in the context of the full *XMM-Newton* validation programme, in which 51 new clusters have been detected. This includes four double and two triple systems, some of which are chance projections on the sky of clusters at different redshifts. We find that association with a source from the RASS-Bright Source Catalogue is a robust indicator of the reliability of a candidate, whereas association with a source from the RASS-Faint Source Catalogue does not guarantee that the SZ candidate is a bona fide cluster. Nevertheless, most *Planck* clusters appear in RASS maps, with a significance greater than $2\sigma$ being a good indication that the candidate is a real cluster. Candidate validation from association with SDSS galaxy overdensity at $z > 0.5$ is also discussed. The full sample gives a *Planck* sensitivity threshold of $Y_{500} \sim 4 \times 10^{-4}$ arcmin$^2$, with indication for Malmquist bias in the $Y_X$–$Y_{500}$ relation below this threshold. The corresponding mass threshold depends on redshift. Systems with $M_{500} > 5 \times 10^{14}$ $M_\odot$ at $z > 0.5$ are easily detectable with *Planck*. The newly-detected clusters follow the $Y_X$–$Y_{500}$ relation derived from X-ray selected samples. Compared to X-ray selected clusters, the new SZ clusters have a lower X-ray luminosity on average for their mass. There is no indication of departure from standard self-similar evolution in the X-ray versus SZ scaling properties. In particular, there is no significant evolution of the $Y_X/Y_{500}$ ratio.

**Key words.** cosmology: observations – galaxies: clusters: general – galaxies: clusters: intracluster medium – cosmic background radiation – X-rays: galaxies: clusters

⋆ Corresponding author: J. Democles, e-mail: jessica.democles@cea.fr

# 1. Introduction

The *Planck*[1] satellite has been surveying the millimetre sky since 2009. Its two instruments together cover nine frequency bands: the Low Frequency Instrument (LFI; Mandolesi et al. 2010; Bersanelli et al. 2010; Mennella et al. 2011) at 30, 44, and 70 GHz, and the High Frequency Instrument (HFI; Lamarre et al. 2010; Planck HFI Core Team 2011) at 100, 143, 217, 353, 545, and 857 GHz. Before the HFI coolant ran out in January 2012, *Planck* had successfully performed nearly 5 surveys of the entire sky.

*Planck* allows the detection of galaxy clusters by their imprint on the cosmic microwave background (CMB) via the Sunyaev-Zeldovich (SZ) effect, a characteristic spectral distortion of the CMB due to inverse Compton scattering of photons by hot electrons in the intra-cluster medium (Sunyaev & Zeldovich 1972). The SZ signal of galaxy clusters is expected to correlate tightly with cluster mass (e.g., da Silva et al. 2004) and its surface brightness is independent of redshift. SZ selected cluster samples are thus particularly well-suited for statistical studies of the galaxy cluster population, either as a probe of the physics of structure formation, or for cosmological studies based on cluster abundance as a function of mass and redshift. Compared to other SZ surveys, such as those with the Atacama Cosmology Telescope (ACT, Marriage et al. 2011) or the South Pole Telescope (SPT, Carlstrom et al. 2011), the *Planck* survey covers an exceptionally large volume; indeed, it is the first all-sky survey since the ROSAT All-Sky Survey (RASS) in the X-ray domain. *Planck* allows the detection of clusters below the flux limit of RASS based catalogues at redshifts typically greater than 0.3 (Planck Collaboration 2012, Fig. 9). The first *Planck* SZ catalogue, the Early SZ (ESZ) sample, was published in Planck Collaboration (2011a). It contains 189 clusters and candidates detected at high signal-to-noise ratio ($S/N > 6$) in the all-sky maps from the first ten months of observations, 20 of which were previously unknown. At the release of the ESZ sample, 12 of those 20 had been confirmed as new clusters, 11 using *XMM-Newton* validation observations undertaken in director's discretionary time (DDT) via an agreement between the *XMM-Newton* and *Planck* project scientists.

All cluster surveys include false detections. For *Planck*, these are mainly due to inhomogeneous, non-isotropic, and highly non-Gaussian fluctuations (galactic dust emission, confusion noise as result of the unsubtracted point sources, etc.) in the complex microwave astrophysical sky. After identification of known clusters, a follow-up programme is required for cluster confirmation and redshift estimation. It is essential to build as pure as possible an initial candidate sample in order for such a programme to be efficient and manageable. For this we rely both on internal *Planck* candidate selection and assessment of the SZ signal quality, and on cross-correlation with ancillary data, as described in Planck Collaboration (2011a). Beyond simple confirmation of new clusters, the *XMM-Newton* validation programme aims to refine this validation process and to yield a better understanding of the new objects that *Planck* is detecting. It consists of snapshot exposures(∼10 ks), sufficient for unambiguous

discrimination between clusters and false candidates (Planck Collaboration 2011b), for a total allocated time of 500 ks for 50 candidates.

In the first two follow-up programmes, described by Planck Collaboration (2011b), we observed 25 candidates in total and helped to define the selection criteria for the ESZ sample. They yielded the confirmation of 17 single clusters, two double systems, and two triple systems[2]. The observations showed that the new clusters are on average less X-ray-luminous and more morphologically disturbed than their X-ray-selected counterparts of similar mass, suggesting that *Planck* may be revealing a non-negligible population of massive, dynamically perturbed objects that are under-represented in X-ray surveys. However, despite their particular properties, the new clusters appear to follow the $Y_{500}-Y_X$ relation established for X-ray selected objects, where $Y_X$, introduced by Kravtsov et al. (2006), is the product of the gas mass and temperature.

In the third follow-up programme, described in Planck Collaboration (2012), we observed 11 candidates with lower SZ detection levels ($4.5 < S/N < 5.3$) than the previous programmes ($5.1 < S/N < 10.6$) in order to investigate the internal SZ quality flags. Probing lower SZ flux than previous campaigns, the third programme also demonstrated the capability of *Planck* to find new clusters below the RASS limit and up to high $z$, including the blind detection at $S/N \sim 5$ of PLCK G266.6−27.3, confirmed by *XMM-Newton* to be an $M_{500} \sim 8 \times 10^{14}\ M_{\odot}$ cluster at $z \sim 1$ (Planck Collaboration 2011d). We also detected tentative evidence for Malmquist bias in the $Y_{SZ}-Y_X$ relation, with a turnover at $Y_{SZ} \sim 4{\times}10^{-4}$ arcmin$^2$.

In the fourth and last *XMM-Newton* validation programme, presented here, we further probe the low SZ flux, high redshift regime. The sample includes 15 candidates, detected at signal-to-noise ratios between 4 and 6.1 in the 15.5-month nominal survey data. We use the results from all *XMM-Newton* validation observations to address the use of ancillary RASS information as an indicator of candidate reliability (Sect. 5). The evolution of cluster SZ/X-ray properties is discussed in Sect. 6. This paper, together with Planck Collaboration (2011b,d, 2012), presents our complete analysis of the DDT *XMM-Newton* validation programme.

We adopt a ΛCDM cosmology with $H_0 = 70\ {\rm km\,s^{-1}\,Mpc^{-1}}$, $\Omega_M = 0.3$, and $\Omega_\Lambda = 0.7$. The factor $E(z) = \sqrt{\Omega_M(1+z)^3 + \Omega_\Lambda}$ is the ratio of the Hubble constant at redshift $z$ to its present-day value. The quantities $M_{500}$ and $R_{500}$ are the total mass and radius corresponding to a total density contrast $\delta = 500$, as compared to $\rho_c(z)$, the critical density of the Universe at the cluster redshift; $M_{500} = (4\pi/3)\,500\,\rho_c(z)\,R_{500}^3$. The SZ flux is characterised by $Y_{500}$, where $Y_{500}\,D_A^2$ is the spherically integrated Compton parameter within $R_{500}$, and $D_A$ is the angular-diameter distance to the cluster. Thus, as defined here, $Y_{500}$ has units of solid angle and is given in arcmin$^2$ in Table 2.

# 2. Sample selection

## 2.1. Planck catalogue

In this paper, candidates were chosen from the catalogue derived from the first 15.5 months of data (the "nominal" mission). The processing status, calibration, and map versions were those of

---

[2] These multiple systems, where more than one cluster contribute to the *Planck* signal, can be either chance association on the sky of clusters at different redshifts, or physically related objects at the same redshift. When referring to double or triple systems in the text, we do not distinguish between the two cases.

**Table 1.** Summary of ancillary information used in selecting candidates for XMM observations, and log of the *XMM-Newton* observations.

| Name | RA$_{SZ}$ (deg) | Dec$_{SZ}$ (deg) | *S/N* | $N_{det}$ | $Q_{SZ}$ | OBSID | Filter | $t_{exp}$ (ks EPN) | Clean fraction (EMOS/EPN) | Category | Confirmed |
|---|---|---|---|---|---|---|---|---|---|---|---|
| PLCK G348.4−25.5 | 291.257 | −49.426 | 6.12 | 3 | A | 0679180101 | t t t | 10.6 | 1.0/0.9 | PHZ | Y |
| PLCK G329.5−22.7$^{†}$ | 278.270 | −65.570 | 5.84 | 3 | B | 0679181501 | m m t | 8.5 | 1.0/1.0 | . . . | Y |
| PLCK G219.9−34.4 | 73.680 | −20.269 | 5.74 | 2 | A | 0679180501 | t t t | 9.5 | 1.0/0.9 | PHZ | Y |
| PLCK G352.1−24.0 | 290.233 | −45.842 | 5.63 | 2 | C | 0679180201 | m m t | 8.5 | 1.0/1.0 | PHZ | Y |
| PLCK G305.9−44.6 | 5.946 | −72.393 | 5.40 | 3 | B | 0679180301 | t t t | 10.1 | 0.4/0.2 | . . . | Y |
| PLCK G196.7−45.5$^{†}$ | 55.759 | −8.704 | 5.21 | 3 | B | 0679180401 | m m m | 9.0 | 1.0/0.8 | . . . | Y |
| PLCK G208.6−74.4 | 30.044 | −24.897 | 5.01 | 3 | B | 0679180601 | t t t | 2.9 | 0.8/0.8 | . . . | Y |
| PLCK G130.1−17.0 | 22.678 | 45.288 | 4.93 | 3 | C | 0679180801 | t t t | 7.5 | 1.0/1.0 | . . . | Y |
| PLCK G239.9−40.0 | 71.683 | −37.029 | 4.76 | 3 | B | 0679181001 | t t t | 9.9 | 1.0/1.0 | . . . | Y |
| PLCK G310.5+27.1 | 201.148 | −35.245 | 4.77 | 2 | B | 0679180901 | t t t | 12.9 | 0.9/0.8 | PHZ | . . . |
| PLCK G196.4−68.3 | 34.921 | −19.263 | 4.73 | 2 | B | 0679181101 | t t t | 11.8 | 0.7/0.4 | PHZ | . . . |
| PLCK G204.7+15.9 | 113.614 | 14.295 | 4.57 | 3 | A | 0679180701 | t t t | 9.4 | 1.0/1.0 | . . . | Y |
| PLCK G011.2−40.4 | 315.233 | −33.107 | 4.47 | 1 | C | 0679181201 | t t t | 8.5 | 1.0/1.0 | PHZ | Y |
| PLCK G147.3−16.6 | 44.099 | 40.291 | 4.41 | 3 | B | 0679181301 | t t t | 10.7 | 0.9/0.6 | PHZ | Y |
| PLCK G210.6+20.4 | 120.218 | 11.093 | 4.01 | 1 | C | 0679181401 | t t t | 8.5 | 1.0/1.0 | SDSS | . . . |

**Notes.** Column (1): *Planck* source name. Columns (2) and (3): right ascension and declination of the Planck source (J2000). Columns (4) and (5): signal-to-noise ratio of the *Planck* cluster candidate detection with the MMF3 algorithm in the *Planck*-maps, and number of methods blindly detecting the candidate. Column (6): quality grade of the SZ detection (A is best). Columns (7)−(10): *XMM-Newton* observation identification number, filter used, on-source exposure time with the EPN camera, and fraction of useful time after cleaning for periods of high background due to soft proton flares (EMOS and EPN camera, respectively). Column (11): category resulting from the pre-selection of the candidates. Column (12): confirmed clusters are flagged. $^{(†)}$ indicates double projected systems.

March 2011. The detection and quality assessment of the cluster candidates followed the general procedure described in Planck Collaboration (2011a). Briefly, a blind cluster search was performed with three methods: the matched multi-frequency filter "MMF3" developed by Melin et al. (2006); an independent matched multi-frequency filter "MMF1"; and the PowellSnakes algorithm (PWS; Carvalho et al. 2009, 2012). Candidates then underwent internal SZ quality checks, removing spurious detections (e.g., association with artefacts or galactic sources), and assessment of the SZ signal detection. The signal assessment included quantitative criteria such as the signal-to-noise ratio and the number of methods blindly detecting the candidate, $N_{det}$, as well as a qualitative assessment based on visual inspection of the frequency maps, reconstructed SZ images, and the frequency spectra for each cluster. The latter procedure is summarised in an SZ quality grade, $Q_{SZ}$, as described in Planck Collaboration (2012).

Previously known clusters were identified via cross-correlation with catalogues and NED/Simbad queries. Possible counterparts were searched for within a 5′ radius of the *Planck* position, allowing us to assign two further external reliability flags:

– association of a FSC (Faint Source Catalogue) or a BSC (Bright Source Catalogue) RASS source (Voges et al. 1999, 2000) or an excess of counts (with corresponding signal-to-noise ratio) in the RASS [0.5−2] keV image;
– galaxy over-density in the Digitized Sky Survey (DSS) red plates[3], from a visual check. In the Sloan Digital Sky Survey (SDSS) area[4], two independent galaxy detection algorithms were applied to the DR7 galaxy catalogues (Fromenteau et al., in prep.; Li & White, in prep.). Both algorithms use photometric redshift information. Quality match criteria were assigned based on cluster richness or the over-density signal-to-noise ratio.

[3] http://stdatu.stsci.edu/dss
[4] http://www.sdss.org

### 2.2. XMM-Newton target selection

The resulting targets are listed together with their SZ quality flags in Table 1. The range of signal-to-noise ratios, $4 < S/N < 6.1$, is wide, with nearly uniform coverage, so that the validation results can be useful for defining the final signal-to-noise ratio for the *Planck* Cluster Catalogue. We considered lower signal-to-noise ratios than the previous validation programme, with 9 targets at $S/N < 5$ and a median $S/N$ of 4.9, as compared to 5.1 previously (for 10.5 months of survey data). A priori, this allows us to reach lower flux or higher redshift. To further push the sample towards high redshift, we discarded candidates with estimated $R_{500}$ size greater than 5′. Although the large positional uncertainty of *Planck* candidates makes the search for a DSS counterpart non-trivial, the brightest galaxies of clusters at $z < 0.5$ are generally visible in DSS (e.g., Fassbender et al. 2011). We thus also used DSS images to select high-$z$ clusters. Half the targets, labelled PHZ (potentially at high $z$) in Table 1, have no visible counterpart in DSS red plates. These are obviously riskier candidates, particularly those with low $N_{det}$ or $Q_{SZ}$.

As previous validation observations have shown, the association of a SZ candidate with a RASS FSC or BSC source is not in itself sufficient to confirm the candidate, as chance association with a point source is always a possibility. Conversely, a candidate with no counterpart in the RASS catalogue may well be a bona fide cluster. With this campaign, in combination with the previous observations, we also aim to address the use of RASS data as an indicator of candidate reliability. In the sample of 36 candidates observed previously, thirteen candidates were associated with a BSC source and seventeen candidates with an FSC source. Only six SZ candidates had no FSC/BSC counterpart, of which the three confirmed candidates were detected in RASS at a signal to noise ratio of $1.7 < S/N < 2.8$. To better span the range of external RASS flags, we chose ten candidates with no FSC or BSC counterpart, six of which correspond to a RASS $S/N < 1.5$. Of the remaining five candidates, only one is associated with a BSC source and four are associated with
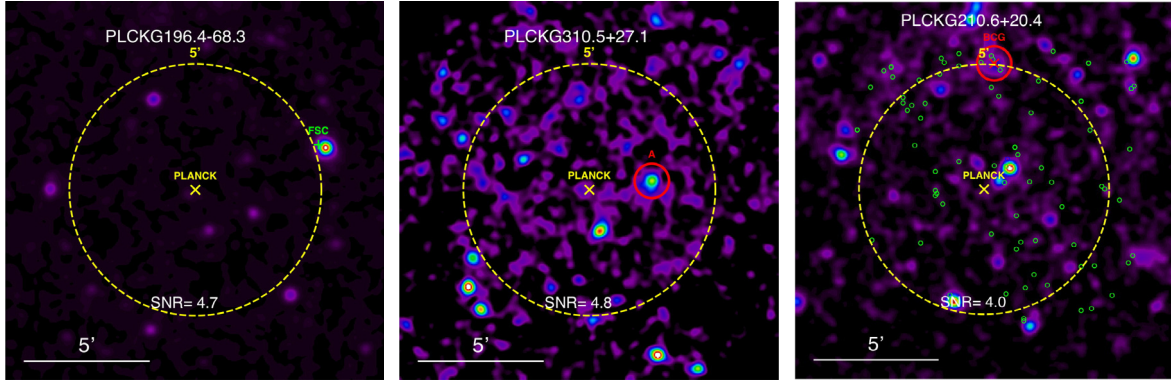
**Fig. 1.** *XMM-Newton* [0.3−2] keV energy band images of the three unconfirmed cluster candidates centred on the SZ position (yellow cross). The red circles indicate the presence of an extended source. Green squares in the *right panel* are positions of galaxies in the SDSS over-density.

with an FSC source. The RASS association for all *XMM-Newton* validation targets is summarised in Table 3.

Finally one candidate, PLCK G210.6+20.4, was specifically chosen to further test our SDSS-based confirmation of very poor SZ candidates. PLCK G210.6+20.4 is the lowest SZ signal-to-noise candidate, detected at $S/N = 4$ by one method only, with a $Q_{SZ} = C$ grade and no significant signal in RASS data. However, the galaxy-detection algorithms (Sect. 2.1) that we used indicated that the candidate is associated with an SDSS galaxy over-density at $z = 0.5$.

## 3. *XMM-Newton* observations and data analysis

Candidates were observed between 31 July 2011 and 13 October 2011. The observation identification number and observation setup are given in Table 1. Due to a slew failure in the satellite revolution 2132, the PLCK G208.6−74.4 observation was incomplete, with an EPN exposure time of 3.4 ks. The target was observed initially at the end of its summer visibility window, and could only be reobserved five months later. It was replaced with an additional visible candidate, PLCK G329.5−22.7.

Calibrated event lists were produced with v11.0 of XMM-SAS. Data that were affected by periods of high background due to soft proton flares were omitted from the analysis (Pratt et al. 2007); clean observing time after flare removal is given in Table 1. The status of each SZ candidate is also given in Table 1: 12 of the 15 candidates are confirmed to be real clusters, among which two are double systems. *XMM-Newton* images of unconfirmed candidates are shown in Fig. 1; confirmed candidates are shown in Fig. 2.

We derived redshifts and physical parameters of the confirmed candidates as described in Planck Collaboration (2011a); Planck Collaboration (2012). Cleaned *XMM-Newton* data were PATTERN-selected. Each photon was then assigned a weight equivalent to the ratio of the effective area at the photon energy and position to the central effective area, computed with SAS task EVIGWEIGHT. Images and spectra were extracted using this weight, assuring full vignetting correction (see Arnaud et al. 2001). Bright point sources were excised from the data and the background was handled as described in Pratt et al. (2010). The particle-induced background (PB) was estimated using a stacked event list built from observations obtained with the filter wheel in closed position. The cosmic X-ray background was modeled using a PB-subtracted spectrum of an annular region external to the cluster emission.

In the spectroscopic analysis, the hydrogen column density was fixed at the 21-cm value of Kalberla et al. (2005). The redshift was estimated by fitting an absorbed redshifted thermal model to the spectrum extracted within a circular region corresponding to the maximum X-ray detection significance. The quality of the $z$ estimate was characterised by the quality flag $Q_z$ as introduced in Planck Collaboration (2011b). $Q_z$ was set to $Q_z = 0$ when the redshift could not be constrained due to the lack of line detection. $Q_z = 1$ corresponds to ambiguous $z_{Fe}$ estimate, when the spectral fit as a function of $z$ exhibited several $\chi^2$ minima that could not be distinguished at the 90% confidence level. $Q_z = 2$ corresponds to a well constrained redshift (i.e., a single $\chi^2$ minimum).

Surface brightness profiles centred on the X-ray peak were extracted from $3\farcs3$ bins in the [0.3−2] keV band for each instrument independently, background subtracted, co-added and rebinned to $3\sigma$ per bin. 3D gas density profile were obtained using the regularised non-parametric method of direct deprojection and PSF deconvolution of the surface brightness profile developed by Croston et al. (2006). Global cluster parameters are estimated self-consistently within $R_{500}$ via iteration about the $M_{500}-Y_X$ relation of Arnaud et al. (2010), assuming standard evolution,

$$E(z)^{2/5}M_{500} = 10^{14.567 \pm 0.010}\left[\frac{Y_X}{2 \times 10^{14}\,M_\odot\,\text{keV}}\right]^{0.561 \pm 0.018}\quad M_\odot.$$

The quantity $Y_X$, is defined as the product of $M_{g,500}$, the gas mass within $R_{500}$, and $T_X$, the spectroscopic temperature measured in the $[0.15−0.75]\,R_{500}$ aperture. In addition, $L_{500}$, the X-ray luminosity inside $R_{500}$, is calculated as described in Pratt et al. (2009). The SZ flux was then re-extracted, $Y_{500}$ being calculated with the X-ray position and size $R_{500}$ fixed to the refined values derived from the high-quality *XMM-Newton* observation. The X-ray properties of the clusters and resulting refined $Y_{500}$ values are listed in Table 2.

## 4. *XMM-Newton* validation outcome

### 4.1. False cluster candidates

For the three candidates shown in Fig. 1, no obvious extended X-ray sources were found within 5′ of the *Planck* position. We followed the maximum likelihood procedure described by Planck Collaboration (2011a) to find all extended sources in the field detected at the $\gtrsim 3\sigma$ level. We then assessed whether they could be the counterpart of the *Planck* candidate from their position and X-ray flux, using the relation between the X-ray flux
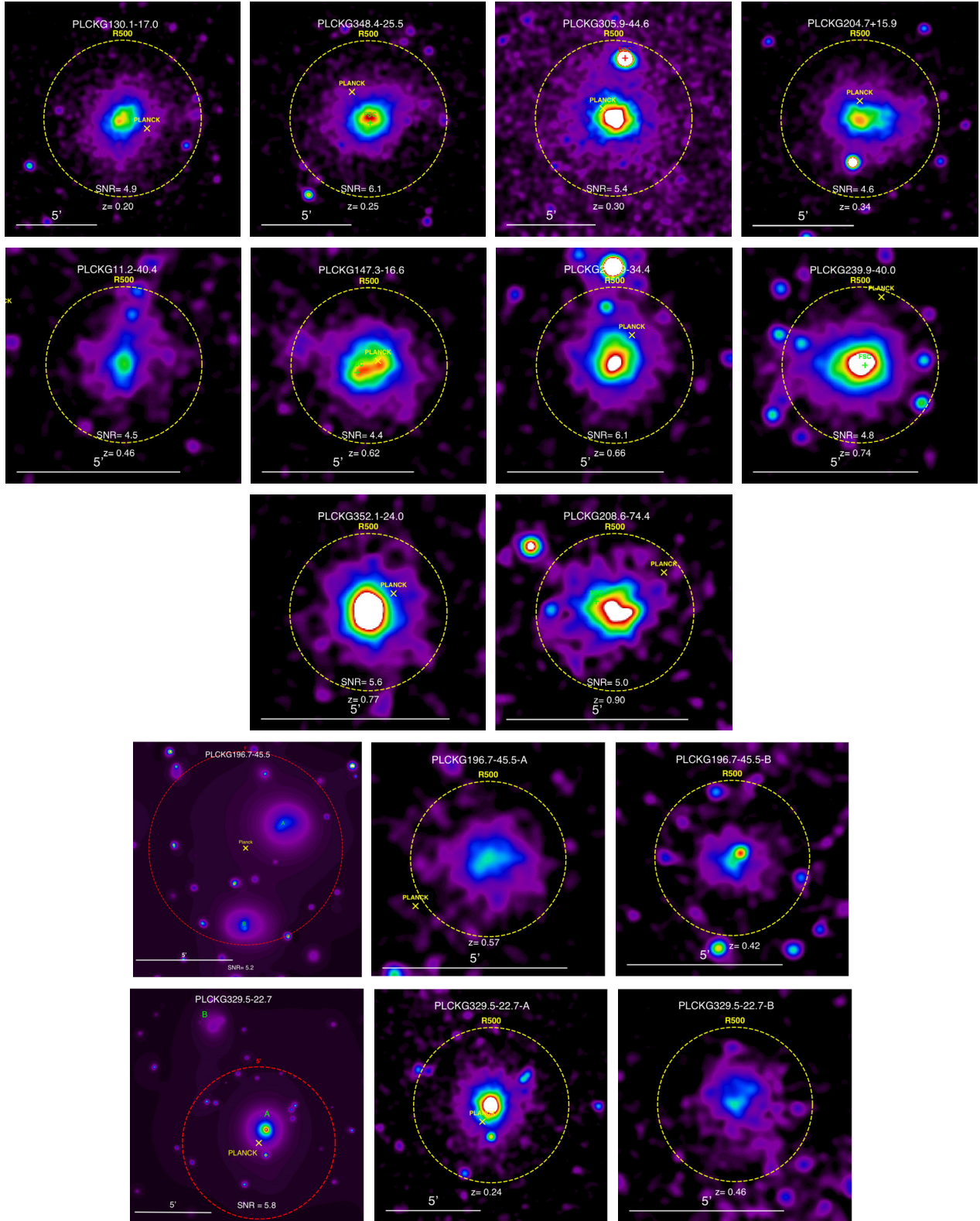
**Fig. 2.** *XMM-Newton* [0.3−2] keV energy band images of confirmed cluster candidates. North is up and East is to the left. Image sizes are $3\theta_{500}$ on a side, where $\theta_{500}$ is estimated from the $M_{500} - Y_{\rm X}$ relation of Arnaud et al. (2010) assuming standard evolution. Images are corrected for surface brightness dimming with $z$, divided by the emissivity in the energy band, taking into account galactic absorption and instrument response, and scaled according to the self-similar model. The colour table is the same for all clusters, so that the images would be identical if clusters obeyed strict self-similarity. A yellow cross indicates the *Planck* position and a red/green plus sign the position of a RASS-BSC/FSC source. The clusters are sorted according their estimated redshift. For the double systems (*last two rows*) the *middle* and *right panels* show the two components and the *left panel* the wavelet-filtered overall image.

**Table 2.** X-ray and SZ properties of the confirmed *Planck* sources.

| Name | $RA_X$ | $Dec_X$ | $z_{Fe}$ | $Q_z$ | $R$ | $\theta_{det}$ | $R_{500}$ | $T_X$ | $M_{gas,500}$ | $Y_X$ | $Y_{500}$ | $M_{500}$ | $L_{500,[0.1-2.4]}$ |
|---|---|---|---|---|---|---|---|---|---|---|---|---|---|
| | [h:m:s] | [d:m:s] | | | [cts s$^{-1}$] | ['] | [kpc] | [keV] | [$10^{14}\,M_\odot$] | [$10^{14}\,M_\odot$ keV] | [$10^{-4}$ arcmin$^2$] | [$10^{14}\,M_\odot$] | [$10^{44}$ erg s$^{-1}$] |
| PLCK G219.9−34.4 | 04:54:45.4 | −20:17:06.6 | 0.66 | 2 | 0.37 ± 0.01 | 2.7 | 1048 | 9.4 ± 1.0 | 0.82 ± 0.03 | 7.7 ± 1.1 | 6.3 ± 1.5 | 6.8 ± 0.5 | 7.3 ± 0.3 |
| PLCK G348.4−25.5 | 19:24:56.1 | −49:27:02.1 | 0.25 | 2 | 1.24 ± 0.02 | 6.4 | 1020 | 5.1 ± 0.2 | 0.47 ± 0.01 | 2.4 ± 0.2 | 8.5 ± 2.0 | 3.9 ± 0.1 | 2.92 ± 0.04 |
| PLCK G352.1−24.0 | 19:20:59.7 | −45:51:02.2 | 0.77 | 1$^\dagger$ | 0.33 ± 0.01 | 2.0 | 925 | 7.8 ± 0.8 | 0.67 ± 0.04 | 5.3 ± 0.9 | 4.0 ± 1.4 | 5.3 ± 0.4 | 10.4 ± 0.3 |
| PLCK G305.9−44.6 | 00:23:38.9 | −72:24:06.1 | 0.30 | 2 | 1.61 ± 0.04 | 6.7 | 1178 | 7.4 ± 0.6 | 0.79 ± 0.02 | 5.8 ± 0.6 | 8.3 ± 2.4 | 6.3 ± 0.4 | 5.9 ± 0.1 |
| PLCK G208.6−74.4 | 02:00:16.4 | −24:54:54.4 | 0.90 | 1 | 0.38 ± 0.01 | 3.2 | 1012 | 11.5 ± 2.4 | 1.02 ± 0.08 | 12. ± 3. | 5.6 ± 1.4 | 8.1 ± 1.3 | 12.6 ± 0.6 |
| PLCK G130.1−17.0 | 01:30:51.3 | +45:17:54.9 | 0.20 | 2 | 1.25 ± 0.02 | 6.3 | 963 | 4.2 ± 0.2 | 0.37 ± 0.01 | 1.6 ± 0.1 | 8.8 ± 2.1 | 3.1 ± 0.1 | 2.04 ± 0.03 |
| PLCK G239.9−40.0 | 04:46:47.2 | −37:03:49.7 | 0.74 | 1$^*$ | 0.56 ± 0.01 | 4.4 | 1033 | 8.4 ± 0.6 | 1.04 ± 0.03 | 8.7 ± 0.9 | 4.4 ± 1.2 | 7.1 ± 0.4 | 11.8 ± 0.2 |
| PLCK G204.7+15.9 | 07:34:27.3 | +14:16:50.2 | 0.34 | 2 | 0.89 ± 0.01 | 4.6 | 1121 | 7.1 ± 0.4 | 0.68 ± 0.02 | 4.9 ± 0.4 | 7.8 ± 2.0 | 5.7 ± 0.2 | 4.20 ± 0.06 |
| PLCK G011.2−40.4 | 21:00:37.6 | −33:08:05.7 | 0.46 | 2 | 0.18 ± 0.01 | 2.9 | 833 | 4.8 ± 0.5 | 0.28 ± 0.02 | 1.4 ± 0.2 | 2.9 ± 1.4 | 2.7 ± 0.2 | 1.78 ± 0.06 |
| PLCK G147.3−16.6 | 02:56:25.3 | +40:17:18.7 | 0.62 | 1$^\spadesuit$ | 0.34 ± 0.01 | 2.4 | 1042 | 8.8 ± 0.8 | 0.76 ± 0.03 | 6.7 ± 0.9 | 5.2 ± 1.7 | 6.3 ± 0.4 | 7.15 ± 0.66 |
| PLCK G329.5−22.7 A | 18:33:00.3 | −65:33:20.0 | 0.24 | 2 | 0.91 ± 0.02 | 4.9 | 917 | 4.4 ± 0.2 | 0.30 ± 0.01 | 1.3 ± 0.1 | … | 2.8 ± 0.1 | 2.16 ± 0.04 |
| PLCK G329.5−22.7 B | 18:33:33.7 | −65:26:39.2 | 0.46 | 2 | 0.25 ± 0.01 | 2.6 | 872 | 4.9 ± 0.7 | 0.35 ± 0.02 | 1.7 ± 0.3 | … | 3.1 ± 0.3 | 2.6 ± 0.1 |
| PLCK G196.7−45.5 A | 03:42:54.2 | −08:40:58.2 | 0.57 | 1$^\ddagger$ | 0.29 ± 0.02 | 5.6 | 820 | 4.4 ± 0.4 | 0.37 ± 0.02 | 1.7 ± 0.2 | … | 2.9 ± 0.2 | 2.8 ± 0.1 |
| PLCK G196.7−45.5 B | 03:43:02.4 | −08:46:09.8 | 0.42 | 1$^\ddagger$ | 0.15 ± 0.01 | 2.4 | 826 | 4.8 ± 0.8 | 0.24 ± 0.02 | 1.2 ± 0.3 | … | 2.5 ± 0.3 | 1.30 ± 0.07 |

**Notes.** Columns (2) and (3): right ascension and declination of the peak of the X-ray emission (J2000). Column (4): redshift from X-ray spectral fitting. Column (5): quality flag for the X-ray redshift measurement (see Sect. 3). Column (6): total EPIC count rates in the [0.3−2] keV band, within the maximum radius of detection given in Col. (7). Columns (8)−(14): $R_{500}$ is the radius corresponding to a density contrast of 500, estimated iteratively from the $M_{500} - Y_X$ relation, $Y_X = M_{g,500}T_X$ is the product of the gas mass within $R_{500}$ and the spectroscopic temperature $T_X$, and $M_{500}$ is the total mass within $R_{500}$. $L_{500,[0.1-2.4]}$ is the luminosity within $R_{500}$ in the [0.1−2.4] keV band. $Y_{500}$ is the spherically integrated Compton parameter measured with Planck, centred on the X-ray peak, interior to the $R_{500}$ estimated with the X-ray observations. Other possible $z_{Fe}$: $^{(\dagger)}$ $z_{Fe} = 0.12, 0.40$; the former solution is excluded from the X-ray versus SZ properties and the latter is unlikely (see Sect. A.1); $^{(*)}$ $z_{Fe} = 0.26, 0.46$. The $z_{Fe} = 0.26$ is unlikely in view of the X-ray versus SZ properties (see Sect. A.1); $^{(\spadesuit)}$ $z_{Fe} = 0.40, 1.03$. The given solution, $z_{Fe} = 0.62$ is that consistent with the optical redshift $z_{spec} = 0.66 \pm 0.05$ (Sect. A.2). $^{(\ddagger)}$ $z_{Fe} = 0.87$ (excluded from DSS red image, see Sect. A.1) and $z_{Fe} = 0.10$ for the A and B components, respectively.

in the [0.1−2.4] keV band, $F_X$, and the SZ flux $Y_{500}$ established by Planck Collaboration (2012):

$$\frac{F_X/10^{-12}\ \mathrm{erg\ s^{-1}\ cm^2}}{Y_{500}/10^{-3}\ \mathrm{arcmin}^2} = 4.95\, E(z)^{5/3}\, (1+z)^{-4}\, K(z). \qquad (1)$$

Here $K = K(z)$ is the $K$ correction, neglecting its temperature dependance.

### 4.1.1. PLCK G196.4−68.3 and PLCK G310.5+27.1

PLCK G196.4−68.3 was classified as PHZ (potentially at high $z$). Analysis of the *XMM-Newton* data on PLCK G196.4−68.3 revealed two extended sources at 9.′9 and 11.′8 from the SZ position. The former corresponds to a RASS-FSC source. Both sources are too far away to be the X-ray counterpart of the *Planck* candidate. A RASS-FSC source is located at 5.′2 from the SZ position and likely contributes to the $S/N = 1.7$ signal derived from RASS data at the *Planck* source location. However, the comparison of its surface brightness profile with the *XMM-Newton* PSF shows that it is consistent with a point source. We thus conclude that PLCK G196.4−68.3 is a false detection.

PLCK G310.5+27.1 was also classified as PHZ. Two extended X-ray sources were detected at 10.′5 and 2.′5 from the SZ position, respectively. The former is too far away to be the X-ray counterpart, while the latter is very weak. Analysis of the surface brightness profile confirmed that it is extended. The detection radius is small, $\theta_{det} = 0.′44$ and the spectrum extracted from this region is too poor to put robust constraints on the redshift or the temperature. However, using the $F_X-Y_{500}$ relation (Eq. (1)) and the measured X-ray flux, we can put an upper limit on $Y_{500}$ assuming a redshift as high as $z = 2$ and taking into account a factor of two dispersion around the relation. For a temperature of $kT = 4$ keV and $z = 2$, we derive a flux within the detection radius of $F_X = 2.8 \times 10^{-14}$ erg s$^{-1}$ cm$^{-2}$.

Assuming that this flux is close to the total, this gives an upper limit on the SZ flux of $Y_{500} \sim 9 \times 10^{-5}$ arcmin$^2$, nearly an order of magnitude smaller than the *Planck* value $Y_{500} \sim 6.7 \pm 1.5 \times 10^{-4}$ arcmin$^2$. Moreover, the SZ significance drops under $2\sigma$ when the flux is re-extracted at the X-ray position. We conclude that this candidate is also a false detection.

Both of these false candidates were detected by two methods, with a medium quality grade of $Q_{SZ} = B$ and at $S/N = 4.7$ and $S/N = 4.8$, respectively. A $Q_{SZ} = B$ quality grade is thus not sufficient to ensure candidate validity at these signal-to-noise ratios. On the other hand, all $Q_{SZ} = A$ candidates down to $S/N = 4.6$ that have been followed up by *XMM-Newton* have been confirmed.

### 4.1.2. PLCK G210.6+20.4

PLCK G210.6+20.4 is associated with an SDSS cluster. The SDSS search algorithm identified a galaxy over-density of 77 members at a photometric redshift of $z \sim 0.57$, consistent with the spectroscopic redshift of the brightest cluster galaxy (BCG) at $z = 0.52$. The barycentre of the concentration and the BCG are located 1.′5 and 5′ from the *Planck* position (see Fig. 1), respectively. The X-ray analysis revealed the presence of an extended source, centred on the BCG, detected at $3.3\sigma$ in the [0.3−2] keV image. However, the source is very faint and more reminiscent of a group of galaxies than of a rich cluster. This is confirmed by the X-ray spectroscopic analysis. Extracting and fitting the spectrum with an absorbed thermal model at $z = 0.52$, we measured a temperature within the detection radius $\theta_{det} = 0.′77$ of $T_{R_{det}} = 1.5 \pm 0.5$ keV and a flux of $F_X = 2.31 \times 10^{-14}$ erg s$^{-1}$ cm$^{-2}$. Using Eq. (1) as above, the upper limit on the corresponding SZ flux is $Y_{500} \sim 2.6 \times 10^{-5}$ arcmin$^2$, more than 10 times lower than the *Planck* value of $4.9 \pm 1.2 \times 10^{-4}$ arcmin$^2$. The X-ray source is too weak to be the *Planck* counterpart and we conclude that the candidate is not a cluster.

In the previous *XMM-Newton* validation run, the two candidates potentially associated with $z > 0.5$ SDSS clusters were confirmed, including PLCK G193.3−46.1 at $z \sim 0.6$. This showed that SDSS can robustly confirm candidates up to such high $z$. It is instructive to compare PLCK G210.6+20.4 with PLCK G193.3−46.1. In both cases the search algorithm found a rich concentration of galaxies, as expected for *Planck* clusters. The masses, reconstructed from the luminosity function, are $\sim 3 \times 10^{14}\ M_\odot$ and $9 \times 10^{14}\ M_\odot$, respectively, i.e., the false candidate has a larger mass. In both cases, the galaxy distribution appears rather loose (compare Fig. 1 right panel and Planck Collaboration 2012, Fig. 5). The *XMM-Newton* observation revealed that PLCK G193.3−46.1 is a double peaked cluster, i.e., a dynamically perturbed cluster with an ICM distribution consistent with the galaxy morphology. In view of the *XMM-Newton* image, the galaxy concentration at the location of PLCK G210.6+20.4 is likely a filamentary structure where only the part around the BCG is virialised and contains gas that is hot enough to emit in X-rays. This would also explain the large offset between the BCG position and the galaxy concentration barycentre, which is much larger than in the case of PLCK G193.3−46.1. These two cases illustrate the difficulty of distinguishing between massive clusters and pre-virialised structures with rather shallow SDSS data at high $z$. Beyond luminosity and mass estimates, important diagnostics include the offset between the SZ, BCG, and barycentre, as well as the galaxy distribution morphology, if available, and other ancillary data, such as significant RASS emission. These factors must all be considered for firm confirmation of low signal-to-noise-ratio SZ detections. On the other hand, we cannot be sure that the apparent SZ signal is purely due to noise, and cannot exclude a contribution from the pre-virialised structure itself, especially if it corresponds to a warm filament along the line of sight.

### 4.2. Confirmed candidates

Twelve of the 15 candidates are confirmed as real clusters, of which two are double systems as shown in Fig. 2. Physical parameters are given in Table 2. For the two double systems, the cluster closest to the *Planck* position is labelled A and the other is labelled B in Table 2.

#### 4.2.1. Single clusters

The redshifts of eight clusters are well constrained by the *XMM-Newton* spectrum (quality flag of $Q_z = 2$). Three of these clusters, PLCK G219.9−34.4, PLCK G011.2−40.4 and PLCK G348.4−25.5 were classified as PHZ. The first two are indeed at $z = 0.46$ and $z = 0.66$, respectively, but PLCK G348.4−25.5 is at $z = 0.25$. Knowing the precise cluster location with *XMM-Newton*, we re-examined the DSS image. A bright galaxy is indeed located exactly at the position of the X-ray peak; however, the field is crowded and there is no obvious galaxy concentration around that BCG. This explains our initial mis-classification.

The redshift determination for three single clusters is more uncertain. There are several $\chi^2$ minima that cannot be distinguished at the 68% confidence level ($Q_z = 1$). As proposed by Planck Collaboration (2012), we used the X-ray versus SZ properties to eliminate unphysical solutions, as well as DSS data. This is detailed in Appendix A.1. The *XMM-Newton* analysis gives three possible redshifts for PLCK G147.3−16.6: 0.4, 0.62, and 1.1, the last being the best-fitting value. The cluster has an interesting double-peaked morphology. It is likely an on-going merger of two nearly equal mass systems (Fig. 3). The analysis
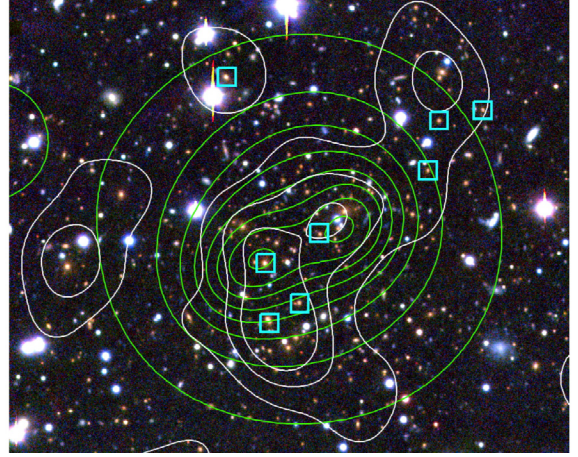


**Fig. 3.** A *gri* composite image of the central $5.'5 \times 3.'4$ of PLCK G147.3−16.6, based on imaging data from NOT/MOSCA (*g* and *i*) and TNG/DOLORES (*r* and *i*). Boxes: cluster galaxies spectroscopically confirmed with Gemini (excluding the two galaxies at $z = 0.68$). North is up and East to the left. The green contours are isocontours of the wavelet filtered *XMM-Newton* image. The white contours show the luminosity distribution of the red sequence galaxies indicated by red symbols in Fig. A.2, smoothed with a $\sigma = 14''$ Gaussian filter. The plotted contour levels are at (10, 20, 30) times the rms variation in the luminosity distribution.

of imaging data obtained with the Telescopio Nazionale Galileo La Palma (TNG) telescope and the Nordic Optical Telescope, as well as spectroscopic data obtained at Gemini, are detailed in Appendix A.2. We confirm a redshift of $z = 0.66 \pm 0.05$.

The spectral analysis of PLCK G208.6−74.4 gives a single $\chi^2$ minimum at $z = 0.9 \pm 0.04$, in very good agreement with SZ versus X-ray properties. However we assign a quality flag of $Q_z = 1$ since the statistical quality of the spectrum is poor due to the short exposure time. Furthermore the DSS image is ambiguous: although there is no visible galaxy at the X-ray maximum, the centroid of the large scale X-ray emission is close to a bright DSS galaxy.

In summary, of the seven candidates we classified as PHZ, two are false, four are indeed at $z \gtrsim 0.5$, and one is at a low redshift of $z = 0.25$. In addition to those clusters which were classified as PHZ, two further $Q_z = 1$ clusters, PLCK G239.9−40.0 and PLCK G208.6−74.4, are most likely at high $z$.

#### 4.2.2. Multiple systems

In PLCK G196.7−45.5, two clusters, separated by $\approx 5.5$ arcmin, lie within the *Planck* position error box: PLCK G196.7−45.5A at $2.'34$ and PLCK G196.7−45.5B at $3.'9$ from the SZ position. In view of the *Planck* resolution, $5'$ to $30'$ depending on frequency (Mennella et al. 2011; Planck HFI Core Team 2011), both clusters certainly contribute to the SZ signal. It is likely a chance association, although given the uncertainty in the redshifts, a binary system cannot be ruled out (see Appendix A.1).

In PLCK G329.5−22.7, the cluster PLCK G329.5−22.7A lies about $1'$ from the *Planck* position, while the second object is about $8'$ away. From the $Y_X$ values and redshift estimates, cluster B is expected to have a $Y_{500}$ flux 1.8 times smaller than that of cluster A, thus contributing 36% to the total flux. Its contribution to the blind signal may differ, as the blind signal is extracted using a single component model found roughly peaked at cluster A. Indeed comparison of such a single component extraction with that using a double component
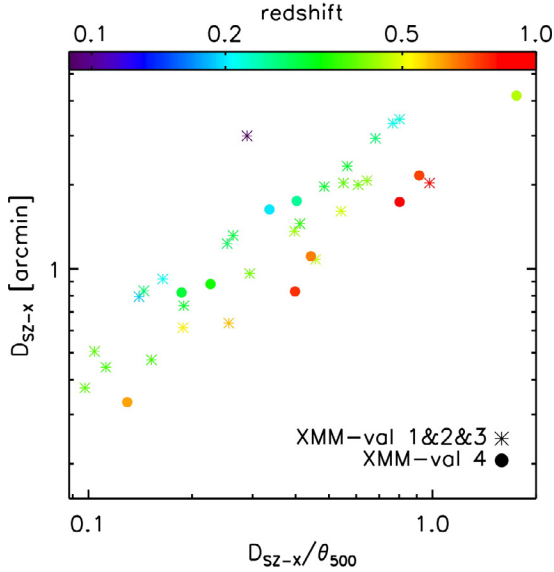
**Fig. 4.** Distance of blind SZ position to X-ray position, $D_{SZ-X}$, as a function of $D_{SZ-X}$, normalised to the cluster size $\theta_{500,X}$ for single confirmed systems. The clusters are colour-coded according to redshift.



**Fig. 5.** Histogram of the distance between the X-ray peak determined from the *XMM-Newton* validation observations and the *Planck* SZ position for all clusters (orange filled) and those associated with a source from the RASS Faint Source Catalogue or Bright Source Catalogue (red hatched). The histogram of the distance between the X-ray peak and the RASS source position is plotted for comparison (blue hatched).

model (with flux ratio fixed to the X-ray constraint) suggests a contamination from cluster B of about ~20%. In summary, PLCK G329.5−22.7 A is the main contributor to the SZ detection, although PLCK G329.5−22.7 B certainly contributes. The redshifts of the two clusters are well determined, $z = 0.24$ and $z = 0.46$, respectively, showing that they are not physically related. This double system is thus a chance association on the sky.

Overall, we have found four double systems and two triple systems among the 43 *Planck* candidates confirmed by *XMM-Newton*, i.e., 14% multiple systems. Since the *XMM-Newton* validation follow-up observations are neither representative nor complete, this fraction of multiple systems cannot be extrapolated to the population at large; however, it is more than five times larger than the fraction of cluster pairs separated by less than 10′ (63/1882 objects) in the whole MCXC X-ray catalogue compilation (Piffaretti et al. 2011). This is clearly a selection effect due to confusion in the large *Planck* beam, which it might be necessary to take into account for a precise estimate of the selection function.

### 4.3. Planck position reconstruction uncertainty

The *Planck* position reconstruction uncertainty is driven by the spatial resolution of the instruments. The positions determined by the *Planck* detection algorithm are compared to the precise *XMM-Newton* positions in Figs. 4 and 5, where we put together all validation observations of single systems. The mean offset between the *Planck* and the *XMM-Newton* position is 1′.5, with a median value of 1′.3, as expected from *Planck* sky simulations (Planck Collaboration 2011a, Fig. 7 left). For 70 and 86% of the clusters, this offset is less than 2′ and 2′.5, respectively. The assumed positional uncertainty of up to 5′ is certainly conservative and an offset of 5′ is actually very unlikely. This needs to be taken into account when searching for possible counterparts in ancillary data or follow-up observations.

The offsets of five sources are greater than 2′.5. Three of those objects are very diffuse, likely dynamically unrelaxed systems, at relatively low $z$, including the prominent outlier PLCK G18.7+23.6 at $z = 0.09$ (Fig. 4, purple point). As noted by Planck Collaboration (2011b) a real, physical offset between
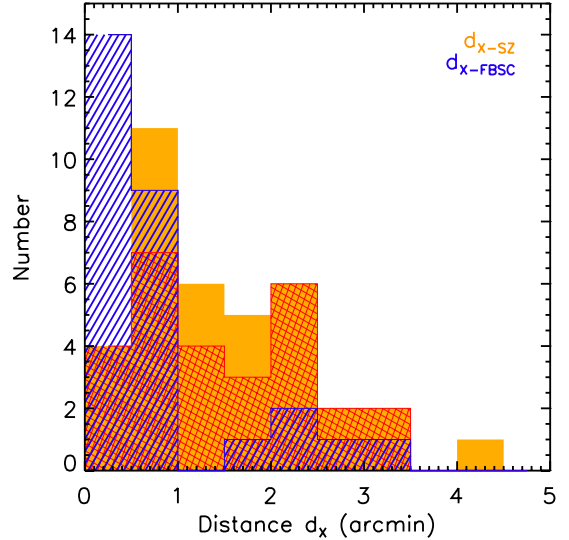
the X-ray and SZ peak may contribute to the overall offset for this type of cluster. In all cases but one, the offset remains smaller than the cluster size $R_{500}$. The notable exception is PLCK G11.2−40.4 (Fig. 4). The *XMM-Newton* position of this cluster is 4′.2 or ~1.8 $R_{500}$ from the *Planck* position. The peak in the SZ reconstructed map is also ~3′ away from from the *Planck* position. This cluster is detected by only one method and has a low quality grade $Q_{SZ}$ = C, being located in a particularly noisy region of the *Planck* map. This is likely to complicate the estimate of the cluster position.

Finally, we note that the position reconstruction uncertainty is on average smaller than for the ESZ sample that peaks at ~2′ (Planck Collaboration 2011a, Fig. 7 right). This is likely the result of the higher redshift range considered here. Indeed, at this redshift the sources are more compact and their position is easier to reconstruct. Furthermore, possible physical offsets are expected to become negligible as they become unresolved.

### 4.4. New clusters in the z–$L_X$ and z–$M_{500}$ plane and Planck sensitivity

The present validation sample covers a wide range of redshift, $0.2 < z < 0.9$, and SZ flux, $2.9 \times 10^{-4}$ arcmin$^2$ < $Y_{500}$ < $8.8 \times 10^{-4}$ arcmin$^2$. As expected from the lower signal-to-noise ratio considered and the deeper sky coverage (Sect. 2), the $Y_{500}$ range is lower than that of the previous validation sample, $4 \times 10^{-4}$ arcmin$^2$ < $Y_{500}$ < $1.4 \times 10^{-3}$ arcmin$^2$. Although not perfect, the strategy to preferentially select high-$z$ clusters was successful, with five clusters found at $z > 0.5$, including three PHZ candidates. The full *XMM-Newton* validation sample (single objects only) is shown in the $L_X$−$z$ plane in Fig. 6. We continue to populate the higher $z$ part of the $L_X$−$z$ plane and confirm *Planck* can detect clusters well below the X-ray flux limit of RASS-based catalogues, ten times lower than REFLEX at high $z$, and below the limit of the most sensitive RASS survey (MACS). The figure makes obvious the gain in redshift coverage as compared to the RASS-based catalogues.
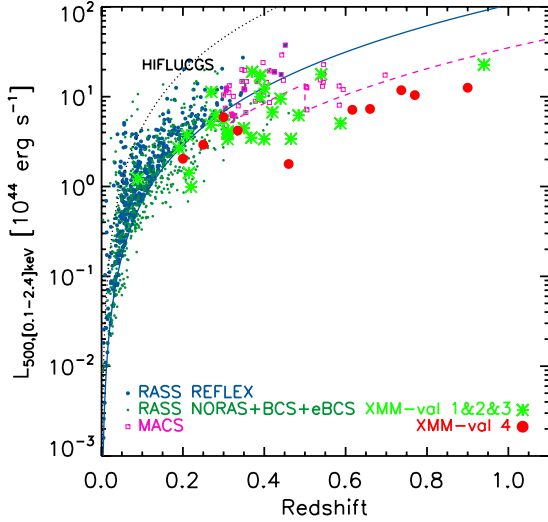
**Fig. 6.** The new SZ-discovered *Planck* single objects compared to clusters from the ROSAT All-Sky Survey catalogues in the $L_X$–$z$ plane. Green points represent *Planck* clusters previously confirmed with *XMM-Newton* (Planck Collaboration 2011b, 2012) and red points are the newly confirmed single clusters. The X-ray luminosity is calculated in the [0.1−2.4] keV band. Catalogues shown are REFLEX (Böhringer et al. 2004), NORAS (Böhringer et al. 2000), BCS (Ebeling et al. 1998), eBCS (Ebeling et al. 2000) and MACS (Ebeling et al. 2007). The solid line is the REFLEX flux limit, the dotted line is the HIFLUCGS flux limit of $2 \times 10^{-11}$ erg s$^{-1}$ cm$^{-2}$ and the dashed line is from the MACS flux limits.

We confirm our previous results on the $Y_{500}$–$Y_X$ relation. Most clusters are consistent with the REXCESS prediction:

$$Y_{500} = 0.924 \, D_A^{-2} \, C_{XSZ} \, Y_X \qquad (2)$$

with $C_{XSZ} = 1.416 \times 10^{-19}$ Mpc$^2$ $M_\odot^{-1}$ keV. However, all clusters below a normalised $Y_X \sim 5 \times 10^{-4}$ arcmin$^2$ lie above the predicted $Y_{500}$–$Y_X$ relation and the bin average deviation increases with decreasing $Y_X$ (Fig. 7). As noted by Planck Collaboration (2012), this is an indication of Malmquist bias.

Figure 8 shows the new *Planck* clusters confirmed with *XMM-Newton* in the $z$–$M_{500}$ plane (single objects only). The minimum mass increases with redshift, an indication of an increase of the mass detection threshold with $z$. Such an increase is expected from the fact that clusters are not resolved by *Planck* at high $z$; however, we clearly confirm that *Planck* can detect $M_{500} > 5 \times 10^{14}$ $M_\odot$ clusters above $z > 0.5$. Two clear outliers in the $z - M$ plane are evident in Fig. 8. They correspond to the lowest flux clusters PLCK G11.2−40.4 and PLCK G268.5−28.1 at $z = 0.46$ and $z = 0.47$, respectively (Fig. 7), lying in the region most affected by the Malmquist bias. PLCK G11.2−40.4 is the cluster mentioned in Sect. 4.3, which is detected with a large offset between the *Planck* position and the X-ray peak, due to its lying in a region with a noisy background. The blind signal is two times higher than the signal extracted at the X-ray position. This is a clear case of a detection boosted by specific local noise conditions.

# 5. Using RASS data in the construction of the *Planck* cluster catalogue

## 5.1. Position refinement

The positions of the associated FSC and BSC source are indicated in the individual *XMM-Newton* image of each candidate
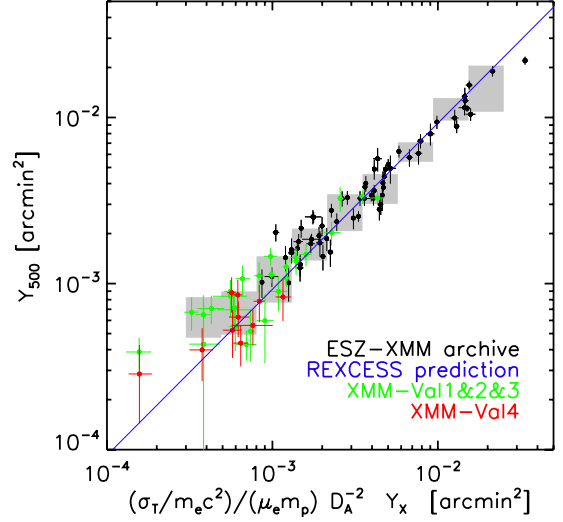


**Fig. 7.** Relation between apparent SZ signal ($Y_{500}$) and the corresponding normalised $Y_X$ parameter for single systems confirmed with *XMM-Newton* (green and red points). Black points show clusters in the *Planck*-ESZ sample with *XMM-Newton* archival data as presented in Planck Collaboration (2011c). The blue lines denote the $Y_{500}$ scaling relations predicted from the REXCESS X-ray observations (Arnaud et al. 2010). The grey area corresponds to median $Y_{500}$ values in $Y_X$ bins with $\pm 1\sigma$ standard deviation.
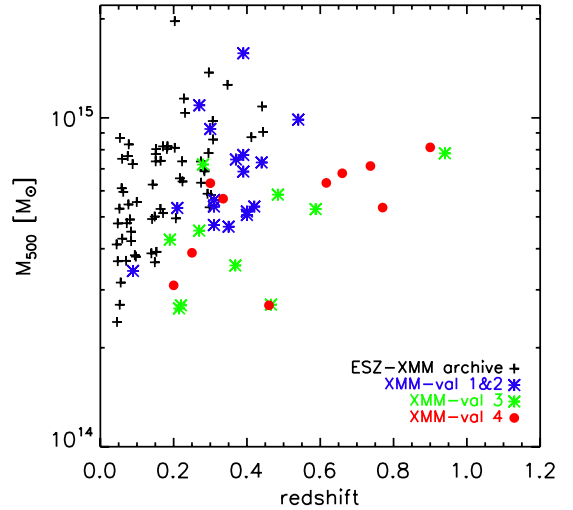


**Fig. 8.** The new SZ-discovered *Planck* single objects (blue, red and green symbols) in the $z$–$M_{500}$ plane. For comparison, black points show known clusters from the ESZ *Planck* catalogue with archival *XMM-Newton* data (Planck Collaboration 2011c). $M_{500}$ are estimated from $Y_X$ and the $M_{500}$–$Y_X$ relation of Arnaud et al. (2010).

in Fig. 2, and for previous observations, in Figs. 3 and 2 published in Planck Collaboration (2011b and 2012). Comparing the positions of the SZ candidates and their FSC/BSC counterparts with the X-ray peaks determined from the *XMM-Newton* validation observations, we notice that the FSC/BSC position is a better estimate of the position of the cluster than the position returned by *Planck* alone. Most of the FSC/BSC sources are located within 1′ of the *XMM-Newton* position versus 2′ for the *Planck*-SZ position (see Fig. 5). Thus, the association with a faint or bright RASS source can be used to refine the SZ position estimate.
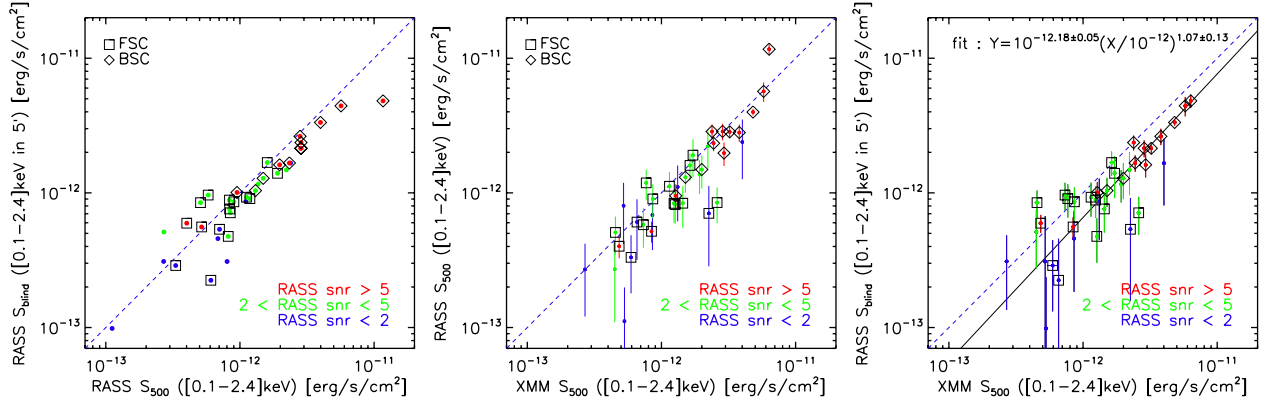
**Fig. 9.** Relations between unabsorbed X-ray fluxes measured in the [0.1−2.4] keV band. Blind fluxes are measured in a 5′ aperture centred on the *Planck* position; all other fluxes are measured in an aperture corresponding to $R_{500}$ centred on the *XMM-Newton* X-ray peak. *Left panel*: blind RASS flux vs RASS flux. *Middle panel*: RASS flux vs. *XMM-Newton* flux. *Right panel*: blind RASS flux vs. *XMM-Newton* flux.

### 5.2. X-ray flux estimate

Figure 9 summarises the comparison between RASS and *XMM-Newton* unabsorbed fluxes computed in the [0.1−2.4] keV band. The *XMM-Newton* flux is given in Table 3. Fluxes measured in an aperture of 5′ centred on the *Planck* candidate position from RASS images are referred to as "blind". Here the RASS count rate is converted to flux assuming a typical redshift of $z = 0.5$, temperature of $kT = 6$ keV, and the 21−cm $N_H$ value. All other fluxes are recomputed in an aperture corresponding to $R_{500}$, centred on the X-ray peak as determined from the *XMM-Newton* validation observations, and using the measured temperature and redshift to convert *XMM-Newton* or RASS count rates to flux.

These figures indicate that the RASS blind fluxes and the RASS fluxes measured within $R_{500}$ are in relatively good agreement, with a slight underestimate at high fluxes (left panel). RASS and *XMM-Newton* fluxes measured within $R_{500}$ are also in relatively good agreement, although with a slight underestimate together with increased dispersion at low fluxes (middle panel). As a result, RASS blind fluxes slightly underestimate the "true" *XMM-Newton* flux measured within $R_{500}$, by ∼30% at $10^{-12}$ erg s$^{-1}$ cm$^{-2}$. The underestimate increases with decreasing S/N (right panel).

In view of this agreement, we conclude that the RASS blind flux can be used to estimate the exposure time required for X-ray follow-up of a *Planck* candidate, once confirmed at other wavelengths. The main limitation is the statistical precision on the RASS estimate.

### 5.3. Candidate reliability

The association of an SZ candidate with a RASS-B/FSC source is neither a necessary nor a sufficient condition for an SZ candidate to be a bona fide cluster. Putting together the results from all *XMM-Newton* validation observations for a total of 51 *Planck* cluster candidates, we find that three of the eight false candidates are associated with an FSC source, while eleven candidates are confirmed without association with a RASS-FSC/BSC source. On the other hand, it is striking that PLCK G266.6−27.3, the most distant cluster of the sample, with a $z = 0.97$, is detected at a S/N > 5 in RASS, and is in fact found in the RASS Faint Source Catalogue.

### 5.3.1. RASS source density

It is important to underline that the RASS is not homogeneous, and that neither the BSC nor the FSC are flux-limited or complete in any way. Using the RASS-BSC and FSC, we computed the source density map of each catalogue and the associated probability that a *Planck* candidate will be associated with a B/FSC source within a radius of 5′. The method is described in Appendix B, and the resulting probabilities are given in Table B.1.

Figures 10 and B.1 show the RASS-FSC and BSC source density maps with all *XMM-Newton* validation observations overplotted. The faint source distribution directly reflects the RASS scanning strategy, as evident in Fig. 10. In this context, the probability of chance association is also an indication of how well covered the region is and thus on the depth of the X-ray observation at this position. We found a mean probability of association with an FSC source of $\mathcal{S}(\mathcal{R} \leq 5') \times \bar{\rho} \sim 6\%$ over the whole sky, where $\mathcal{S}(\mathcal{R} \leq 5')$ is the area corresponding to a circle of 5′ and $\bar{\rho}$ is the mean density at the position of the candidate, respectively. The corresponding mean probability of association with a BSC source is ∼1%. However, in the best-covered regions of the RASS the probability can reach 95% for the FSC and 9% for the BSC, while in the least-covered regions these probabilities drop to 0.4% and 0.2%, respectively.

### 5.3.2. BSC source association

All 12 candidates associated with a BSC source are confirmed. This is not surprising. For the BSC, the probability of chance association is relatively low, varying from less than 1% to 9%, depending on the sky region. For one cluster, PLCKG305.9−44.6, the *XMM-Newton* validation observation reveals that a point source is located at the position of the BSC source. However, the source is labelled as extended in the BSC, and in fact the X-ray emission likely corresponds to a blend of the point source and extended cluster emission that was not resolved with the large ROSAT PSF. This is supported by a comparison of the *XMM-Newton* and RASS images.

Thus we conclude that the correspondence of a *Planck* SZ candidate with a RASS-BSC source is a very good indication of there being a real cluster at this position.

### 5.3.3. FSC source association

For the FSC catalogue, on the contrary, the conclusion is more uncertain because of the larger probability of chance association. Most (18 of 21, i.e., more than 85%) of the candidates associated with a faint source are indeed confirmed. For the

**Table 3.** RASS information for single confirmed clusters and false candidates.

| Name | S/N | $S_{500,XMM}$ | Ass. | Run | Confirmed |
|---|---|---|---|---|---|
| | RASS | $10^{-12}$ erg s$^{-1}$ cm$^{-2}$ | | | |
| PLCK G271.2−31.0 | 18.4 | 4.82 ± 0.03 | B | 2 | Y |
| PLCK G286.6−31.3 | 10.7 | 3.23 ± 0.07 | B | 2 | Y |
| PLCK G018.7+23.6 | 8.8 | 6.35 ± 0.09 | B | 2 | Y |
| PLCK G305.9−44.6 | 7.9 | 2.38 ± 0.05 | B | 4 | Y |
| PLCK G234.2−20.5 | 7.2 | 2.45 ± 0.02 | B | 3 | Y |
| PLCK G285.0−23.7 | 7.1 | 3.80 ± 0.04 | B | 2 | Y |
| PLCK G060.1+15.6 | 7.0 | 2.86 ± 0.06 | B | 3 | Y |
| PLCK G268.5−28.1 | 6.6 | 0.48 ± 0.02 | F | 3 | Y |
| PLCK G171.9−40.7 | 6.1 | 5.78 ± 0.06 | B | 2 | Y |
| PLCK G266.6−27.3 | 5.6 | 0.84 ± 0.02 | F | 3 | Y |
| PLCK G241.2−28.7 | 5.1 | 1.28 ± 0.02 | B | 2 | Y |
| PLCK G019.1+31.2 | 5.1 | 2.93 ± 0.04 | B | 3 | Y |
| PLCK G277.8−51.7 | 4.9 | 1.63 ± 0.03 | F | 1 | Y |
| PLCK G208.6−74.4 | 4.3 | 0.45 ± 0.02 | F | 4 | Y |
| PLCK G250.0+24.1 | 4.2 | 0.73 ± 0.04 | F | 1 | Y |
| PLCK G286.3−38.4 | 4.1 | 1.51 ± 0.04 | B | 1 | Y |
| PLCK G285.6−17.2 | 3.8 | 1.24 ± 0.02 | F | 2 | Y |
| PLCK G130.1−17.0 | 3.7 | 1.92 ± 0.03 | | 4 | Y |
| PLCK G200.9−28.2 | 3.7 | 0.77 ± 0.03 | F | 3 | Y |
| PLCK G235.6+23.3 | 3.6 | 0.86 ± 0.02 | F | 3 | Y |
| PLCK G262.2+34.5 | 3.5 | 1.15 ± 0.02 | F | 3 | Y |
| PLCK G004.5−19.5 | 3.3 | 2.00 ± 0.03 | B | 1 | Y |
| PLCK G272.9+48.8 | 3.2 | 2.60 ± 0.10 | F | 2 | Y |
| PLCK G205.0−63.0 | 3.0 | 1.44 ± 0.02 | F | 2 | Y |
| PLCK G348.4−25.5 | 2.9 | 1.72 ± 0.02 | F | 4 | Y |
| PLCK G292.5+22.0 | 2.8 | 2.22 ± 0.04 | | 2 | Y |
| PLCK G100.2−30.4 | 2.8 | 1.27 ± 0.03 | F | 2 | Y |
| PLCK G226.1−16.9 | 2.3 | … | F | 1 | … |
| PLCK G193.3−46.1 | 2.2 | 0.45 ± 0.01 | F$^{\dagger}$ | 3 | Y |
| PLCK G204.7+15.9 | 2.0 | 1.32 ± 0.02 | | 4 | Y |
| PLCK G287.0+32.9 | 1.9 | 4.01 ± 0.05 | | 2 | Y |
| PLCK G147.3−16.6 | 1.8 | 0.59 ± 0.06 | F | 4 | Y |
| PLCK G011.2−40.4 | 1.8 | 0.27 ± 0.01 | | 4 | Y |
| PLCK G210.6+17.1 | 1.7 | 0.86 ± 0.01 | | 3 | Y |
| PLCK G196.4−68.3 | 1.7 | … | | 4 | … |
| PLCK G070.8−21.5 | 1.6 | … | | 1 | … |
| PLCK G262.7−40.9 | 1.3 | 2.26 ± 0.02 | F | 2 | Y |
| PLCK G113.1−74.4 | 1.2 | … | F | 3 | … |
| PLCK G343.4−43.4 | 1.2 | … | F | 1 | … |
| PLCK G239.9−40.0 | 1.0 | 0.66 ± 0.01 | F | 4 | Y |
| PLCK G352.1−24.0 | 0.7 | 0.52 ± 0.01 | | 4 | Y |
| PLCK G219.9−34.4 | 0.7 | 0.53 ± 0.02 | | 4 | Y |
| PLCK G317.4−54.1 | −0.4 | … | | 1 | … |
| PLCK G310.5+27.1 | −0.9 | … | | 4 | … |
| PLCK G210.6+20.4 | −1.0 | … | | 4 | … |

**Notes.** (1) Name of the candidate. (2) Signal-to-noise ratio of the RASS count rate in the [0.5−2] keV band, measured within a region of 5′ radius centred on the SZ candidate position. (3) Flux in the [0.1−2.4] keV band as measured with *XMM-Newton* within $\theta_{500}$. (4) Association with a source from the RASS Faint Source Catalogue (F) or Bright Source catalogue (B) published by Voges et al. (1999, 2000). (5) Number of the *XMM-Newton* validation run. (6) Confirmed clusters are flagged. $^{(\dagger)}$ The FSC source is not the cluster.

triple system PLCK G214.6+36.9, the FSC source is classified as extended. Its position as given in the RASS catalogue lies between the three clusters and is close to that of a bright *XMM-Newton* point source. The FSC source is thus in fact a blend of the cluster(s) and of the point source. In only one case, PLCK G193.3−46.1, does the FSC not correspond to the cluster emission. The *XMM-Newton* and RASS data shows that it is a point source located 3.′3 away from the cluster centre.

Taking into account PLCK G193.3−46.1 and the three false candidates associated with an FSC source, we found four cases of mis-associations out of 51 candidates, i.e., 8%. This is

consistent with the mean probability of chance association of 6% computed above; however, the association with an FSC source is still an indicator of reliability even in the regions of high probability of chance association. For instance, the two highest-redshift clusters ($z \approx 0.9$) are correctly associated with a faint source, despite both being in the ecliptic pole region where the probability of false association is high. The scanning strategies of *Planck* and RASS are very similar in that both surveys are deeper in the same regions. In well-covered regions, the association with the faint source catalogue allows us to probe less massive or higher redshift potential clusters. A possible indicator of false association might be the distance between the FSC source and the SZ position, although no strict criterion can be applied. Seventy-five per cent of the false associations correspond to a distance greater than 3′, compared to 2 out of 16 (13%) for true associations.

### 5.3.4. No association

Sixteen candidates are not associated with a B/FSC source. Five of these candidates are false and eleven candidates are true sources with no B/FSC source association. As mentioned above, the association with a B/FSC is not necessary for an SZ candidate to be a bona fide cluster. However, we note that the median probability of FSC chance association, a measure of survey depth as discussed Sect. 5.3.1, is 2.1% for clusters without association, to be compared to 6.7% for associated clusters (see also Fig. 10). These true clusters with no B/FSC counterpart are located in the shallower part of the RASS survey, which likely explains why they are not associated.

### 5.3.5. RASS flux and signal-to-noise limit for candidate validation

Unassociated and associated candidates follow the same general correlation between the RASS blind flux, $F_X$, and the SZ flux, $Y_{500}$ (Fig. 11). This correlation presents some dispersion, with deviations from the mean as large as a factor of three. This is expected from the large statistical errors, as well as from the intrinsic dispersion and $z$ dependence of the $F_X/Y_{500}$ ratio (Planck Collaboration 2012) and the difference between the blind and true X-ray fluxes (Sect. 5.2).

Because of this large dispersion, it is not possible to determine a strict RASS flux (or signal-to-noise ratio) limit below which a candidate should be discarded. However, we note that all new clusters have an X-ray flux greater than ∼2 × $10^{-13}$ erg s$^{-1}$ cm$^{-2}$ (grey area in Fig. 11). This flux is consistent with the $Y_{500}$ threshold $Y_{500,\mathrm{thresh}} \approx 2-5 \times 10^{-4}$ arcmin$^2$, as defined from the region affected by the Malmquist bias (see Fig. 7). This RASS flux limit is more than 10 times lower than the REFLEX flux limit of ∼2 × $10^{-12}$ erg s$^{-1}$ cm$^{-2}$, but still detectable with RASS[5]. For the confirmed candidates, the minimum signal-to-noise ratio computed from RASS data is ∼0.70. Below that limit, all the candidates were false. All candidates with RASS $S/N > 3$ are confirmed, and only one false candidate is found for RASS $S/N > 2$. The latter is an SZ candidate detected at low *Planck S/N* = 4.

---

[5] Such clusters, however, could not be identified from RASS data alone. They cannot be identified as clusters on the basis of source extent because of the low statistical quality of the signal. Confirmation and identification follow-up is unmanageable in view of the number of sources at such low flux, the vast majority of which are unidentified AGN or noise fluctuations.
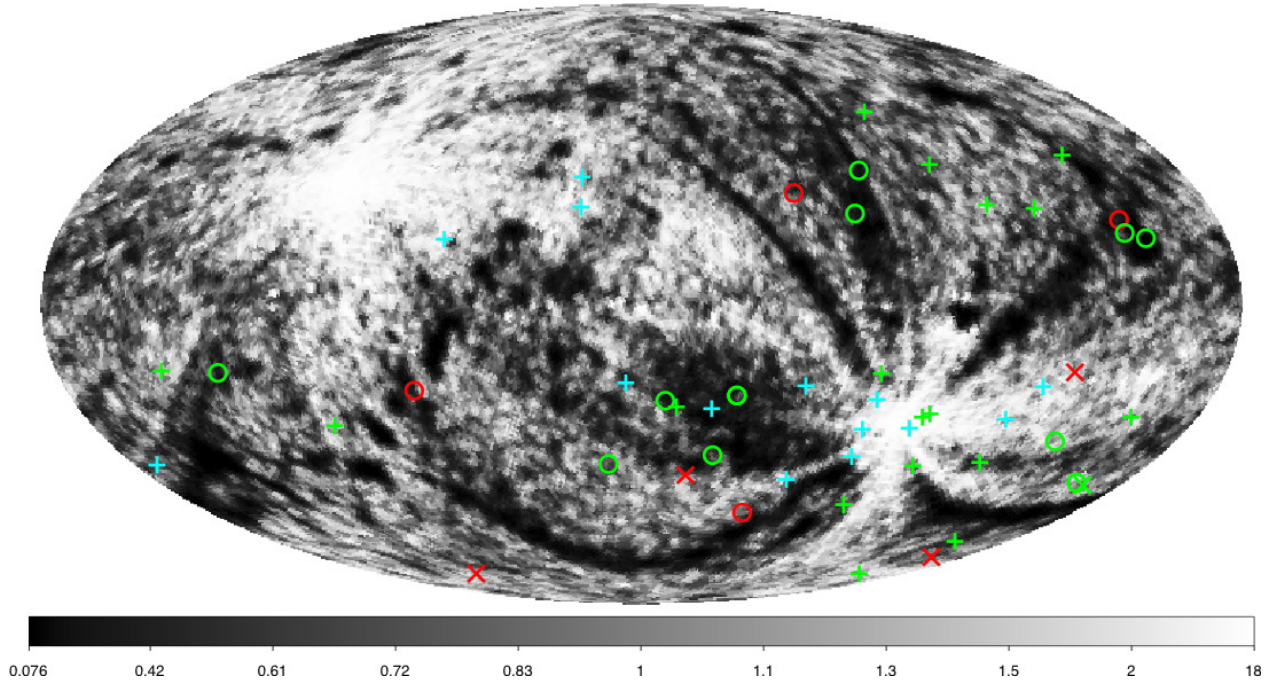
**Fig. 10.** Density map of the RASS-Faint Source Catalogue (FSC) with *XMM-Newton* validation results overplotted. The source density map has been normalised by the median of the pixel density distribution. The source density directly reflects the RASS scanning strategy, with the largest exposure and source density at the Ecliptic poles. Cyan pluses (+): confirmed candidates associated with a BSC source. Other confirmed candidates are plotted in green, and false candidates are plotted in red. Pluses (+): good association with a FSC source. Crosses (×): mis-association with an FSC source. Circles (○): no association with a FSC/BSC source. Confirmed candidates with no association are mostly located in low density regions corresponding to the shallower part of the RASS survey.
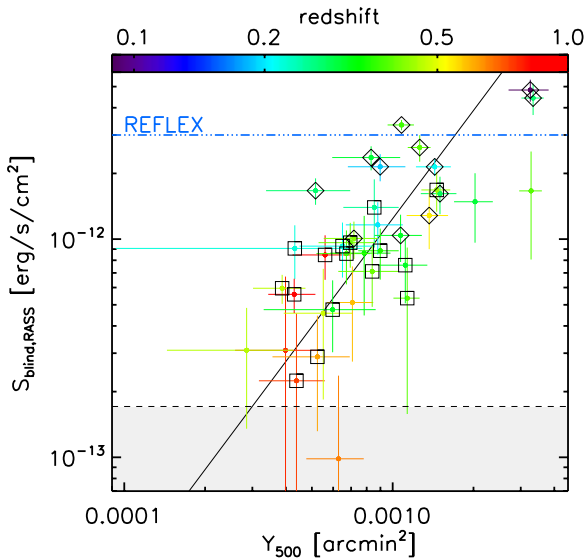


**Fig. 11.** Relation between RASS blind fluxes and SZ fluxes, $Y_{500}$, for single systems confirmed with *XMM-Newton* (all validation observations). The RASS flux is the unabsorbed flux computed in the [0.1−2.4] keV band and measured in a 5′ aperture centred on the *Planck* position. The points are colour-coded as a function of redshift. Squares are candidates associated with a FSC source while diamonds are candidates associated with a BSC source.

### 5.3.6. RASS reliability flag

In view of the above results, we conclude the following regarding the most relevant RASS reliability flags:

- positional association of a *Planck* SZ candidate with a RASS-BSC source is a very strong indication that the candidate is a cluster;

- positional association of a *Planck* SZ candidate with a RASS-FSC source at $S/N > 2$ is a good indication of a real cluster;
- an SZ candidate with no signal at all in RASS is false at very high confidence. Obviously, candidates with low signal-to-noise ratio in a well-covered region are particularly likely to be false.

## 6. A preview of cluster evolution

With this new *XMM-Newton* validation campaign, we have now assembled a sample of 37 new single *Planck* clusters covering a redshift range $0.09 < z < 0.97$. With only snapshot *XMM-Newton* observations, the global properties and density profile of each object are measured accurately enough to allow a first assessment of evolution with redshift. The structural and scaling properties of the sample are illustrated in Fig. 12. We considered three redshift bins, $z < 0.3$ (10 clusters), $0.3 < z < 0.5$ (19 clusters) and $z > 0.5$ (8 clusters). We confirm our previous finding regarding the scaling properties of these new *Planck* selected clusters, and do not find any evidence of departure from standard self-similar evolution.

The average scaled density profile (top left panel of Fig. 12) is similar for each $z$ bin and is flatter than that of REXCESS, a representative sample of X-ray selected clusters (Arnaud et al. 2010). Once scaled as expected from standard evolution, the new clusters in each redshift bin follow the same trends in scaling properties (Fig. 12): they are on average less luminous at a given $Y_{500}$, or more massive at a given luminosity, than X-ray selected clusters. On the other hand, they follow the $Y_{500}-Y_X$ relation predicted from REXCESS data (Eq. (2)).

To study possible evolution with $z$, we plot in Fig. 13 the $D_A^2 Y_{500}/C_{XSZ} Y_X$ ratio as function of $z$, including the 62 clusters of the *Planck*-ESZ sample with *XMM-Newton* archival data
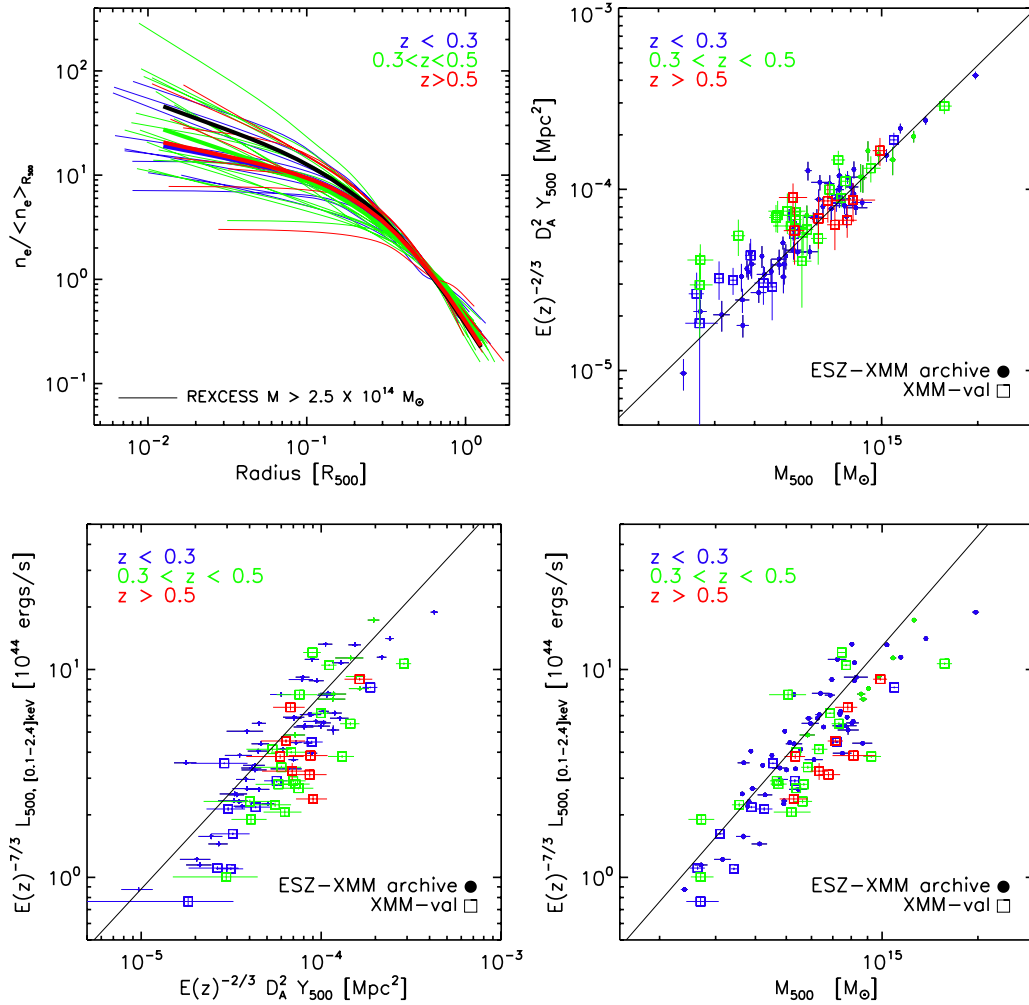
**Fig. 12.** Scaling properties of *Planck* clusters, colour-coded as a function of redshift. In all figures, $R_{500}$ and $M_{500}$ are estimated from the $M_{500}-Y_X$ relation of Arnaud et al. (2010). *Top left panel*: the scaled density profiles of the new clusters confirmed with *XMM-Newton* observations. The radii are scaled to $R_{500}$. The density is scaled to the mean density within $R_{500}$. The thick lines denote the mean scaled profile for each sub-sample. The black line is the mean profile of the REXCESS sample (Arnaud et al. 2010). *Other panels*: scaling relations. Squares show the new clusters confirmed with *XMM-Newton* observations. Points show clusters in the *Planck*-ESZ sample with *XMM-Newton* archival data as presented in Planck Collaboration (2011c). Relations are plotted between the intrinsic Compton parameter, $D_A^2 Y_{500}$, and the mass $M_{500}$ (*top right panel*), between the X-ray luminosity and $Y_{500}$ (*bottom left panel*) and between mass and luminosity (*bottom right panel*). Each quantity is scaled with redshift, as expected from standard self-similar evolution. The lines in the left and middle panel denotes the predicted $Y_{500}$ scaling relations from the REXCESS X-ray observations (Arnaud et al. 2010). The line in the right panel is the Malmquist bias corrected $M-L$ relation from the REXCESS sample (Pratt et al. 2009; Arnaud et al. 2010). The new clusters are on average less luminous at a given $Y_{500}$, or more massive at a given luminosity, than X-ray selected clusters. There is no evidence of non-standard evolution.

(Planck Collaboration 2011c). We exclude clusters at low flux, $D_A^{-2} C_{XSZ} Y_X < 5 \times 10^{-4}$ arcmin$^2$, to minimise possible Malmquist bias (see Sect. 4.4). The best fitting power law gives a slope $\alpha = 0.043 \pm 0.036$, with a normalisation of $0.97 \pm 0.03$ at $z = 0.2$. The relation is thus consistent with a constant ratio at the REXCESS value of $0.924 \pm 0.004$. A histogram of the ratio shows a peak exactly at the REXCESS position. The distribution is skewed towards high ratios, the skewness decreasing if low flux clusters are excluded. This skewness might be intrinsic to the cluster population. It might also reflect a residual effect of the Malmquist bias, clusters with intrinsic high $Y_{500}/Y_X$ ratio being preferentially detected in SZ surveys.

## 7. Conclusions

We have presented results on the final 15 *Planck* galaxy cluster candidates observed as part of a 500 ks validation programme undertaken in *XMM-Newton* Director's Discretionary

Time. The sample was derived from blind detections in the full 15.5-month nominal *Planck* survey, and includes candidates detected at $4.0 < S/N < 6.1$. External flags including RASS and DSS detection were used to push the sampling strategy into the low-flux, high-redshift regime and to better assess the use of RASS data for candidate validation. This last phase of the follow-up programme yielded 14 clusters from 12 *Planck* candidate detections (two candidates are double systems) with redshifts between 0.2 and 0.9, with six clusters at $z > 0.5$. Their masses, estimated using the $M_{500}-Y_X$ relation, range from $2.5 \times 10^{14}$ to $8 \times 10^{14}$ $M_\odot$. We found an interesting double peaked cluster, PLCK G147.3−16.6, that is likely an ongoing major merger of two systems of equal mass. Optical observations with NOT, TNG, and Gemini confirmed a redshift of 0.65.

The full *XMM-Newton* validation follow-up programme detailed in this paper and in Planck Collaboration (2011b); Planck Collaboration (2012) comprises 51 observations of *Planck*
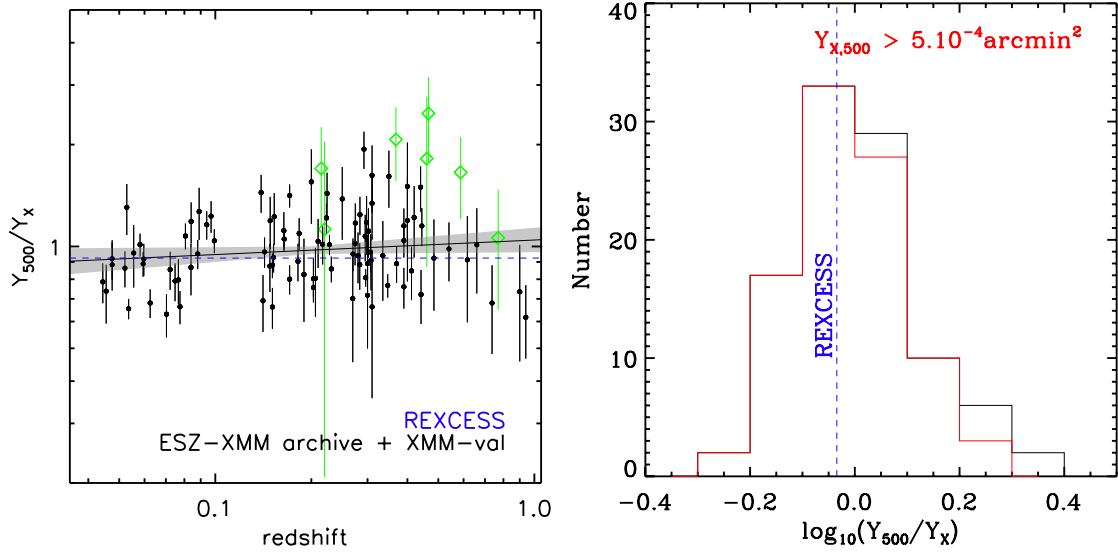
**Fig. 13.** Ratio of the $Y_{500}$ Compton parameter to the normalised $Y_X$ parameter. *Left panel*: variation as a function of redshift. The dotted line is the REXCESS prediction (Arnaud et al. 2010). The full line is the best fit power law and the grey shaded area indicates the $\pm 1\sigma$ uncertainty. Clusters with normalised $Y_X \lesssim 5 \times 10^{-4}$ arcmin$^2$ (green points) were excluded from the fit, to minimise Malmquist bias. *Right panel*: histogram of the ratio without and with low flux clusters.

cluster candidates. The efficiency of validation with *XMM-Newton* stems both from its high sensitivity, allowing easy detection of clusters in the *Planck* mass and redshift range, and from the tight relation between X-ray and SZ properties, which probe the same medium. The search for extended *XMM-Newton* emission and a consistency check between the X-ray and SZ flux is then sufficient for unambiguous discrimination between clusters and false candidates. We have confirmed the relation between the X-ray flux and the SZ flux, as a function of redshift, and estimated its typical scatter. This relation is used in the validation procedure. By contrast, optical validation is hampered by the relatively large *Planck* source position uncertainty and the large scatter between the optical observables (such as galaxy number) and the mass (or SZ signal), both of which increase the chance of false associations.

The programme yielded 51 bona fide newly-discovered clusters, including four double systems and two triple systems. There are eight false candidates. Thirty-two of the 51 individual clusters have high quality redshift measurements from the Fe K line. For other cases, the spectral fitting yields several $\chi^2$ minima as a function of $z$, that cannot be distinguished at the 68% confidence level. We showed that the relation between the X-ray and SZ properties can be used to further constrain the redshift. The new clusters span the redshift range 0.09 to 0.97 and cover more than one decade in $Y_{500}$, from $2.9 \times 10^{-4}$ to $3.0 \times 10^{-3}$ arcmin$^2$. $M_{500}$ of single systems is in the range $(2.5 \times 10^{14} - 1.6 \times 10^{15})\, M_\odot$. These observations provided a first characterisation of the new objects that *Planck* is detecting:

– The newly-detected clusters follow the $Y_X$–$Y_{500}$ relation derived from X-ray selected samples. This is consistent with the prediction that both quantities are tightly related to the cluster mass.
– New SZ selected clusters are X-ray underluminous on average compared to X-ray selected clusters, and more morphologically disturbed. The dispersion around the $M$–$L_X$ relation may be larger than previously thought and dynamically perturbed (merging) clusters might be under-represented in X-ray surveys. This has implications for

statistical studies of X-ray selected samples, either to constrain cosmological models from cluster number counts or to probe the physics of structure formation from the cluster scaling properties. As discussed in detail by Angulo et al. (2012), precise knowledge of the actual scatter between the mass and the observable used in the detection is critical in both applications.
– We found no indication of departure from standard self-similar evolution in the X-ray versus SZ scaling properties. In particular, there is no significant evolution of the $Y_X/Y_{500}$ ratio.

Beyond new cluster confirmation and characterisation, we checked the pertinence of the validation process based on *Planck* internal quality assessments and cross-correlation with ancillary data. There are eight false candidates in total, all of which were found at $S/N < 5$. These failures underline the importance of the number of methods detecting the clusters and were used to refine our internal quality flag definitions. All candidates with $Q_{SZ} = A$ are confirmed. Galaxy overdensity in SDSS data can confirm candidates up to $z \sim 0.6$, although it remains difficult to distinguish between massive clusters and pre-virialised structures at high $z$. The quality of the SZ detection, ancillary data such as significant RASS emission, and the offsets between SZ, BCG, and other positions, must all be considered for firm confirmation. Using the full sample of 51 observations, we investigated the use of RASS-based catalogues and maps for *Planck* catalogue construction, finding that:

– *Planck* clusters appear almost always to be detectable in RASS maps, although there is not a one-to-one correspondence between a RASS-BSC or FSC source and the presence of a cluster.
– Association of a cluster candidate with a RASS-BSC source is a very strong indication that it is a real cluster.
– Whether or not there is a RASS-BSC or FSC source, $S/N > 2$ in the RASS maps is a good indication of a true candidate, while $S/N < 0$ is a good indication of a false candidate.
– The association with a faint or bright RASS source can be used to refine the SZ position estimate. The RASS blind flux

can be used to estimate the exposure time required for X-ray follow-up of a *Planck* candidate, once confirmed at other wavelengths. The main limitation is the statistical precision on the RASS estimate.

The *XMM-Newton* validation observations could also be used for the verification of *Planck* performances, showing that:

– The mean offset between the *Planck* position and the cluster position is $1.'5$, as expected from *Planck* sky simulations, and this offset is less than $2.'5$ for 86% of the clusters.
– *Planck* can detect clusters well below the X-ray flux limit of RASS based catalogues, ten times lower than REFLEX at high $z$, and below the limit of the most sensitive RASS survey (MACS).
– The *Planck* sensitivity threshold for the nominal survey is $Y_{500} \sim 4 \times 10^{-4}$ arcmin$^2$, with an indication of Malmquist bias in the $Y_X - Y_{500}$ relation below this threshold. The corresponding mass threshold depends on redshift, but *Planck* can detect systems with $M_{500} > 5 \times 10^{14} M_\odot$ at $z > 0.5$.
– Overall, there is a high fraction of double/triple systems in the *XMM-Newton* validation follow-up sample, illustrating the problems of confusion in the *Planck* beam.

These results illustrate the potential of the all-sky *Planck* survey to detect the most massive clusters in the Universe. Their characterisation, and the determination of their detailed physical properties, depends on a vigorous follow-up programme, which we are currently undertaking.
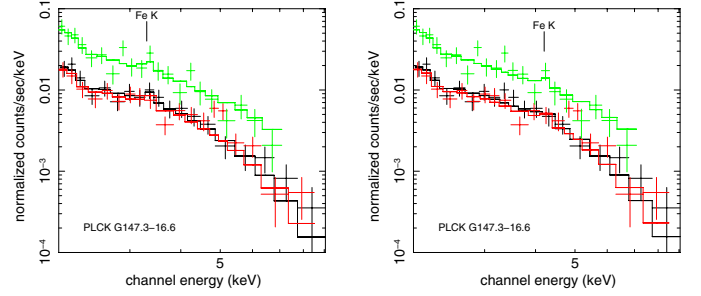
**Fig. A.1.** EPIC spectra (data points with errors) of PLCK G147.3−16.6. Only data points above 2 keV are shown for clarity, but data down to 0.3 keV are used in the spectral fitting. The redshift estimate is ambiguous, with the $\chi^2$ distribution showing three minima. *Left panel*: the best-fitting thermal model (solid lines) at $z = 1.03$ with the position of the redshifted Fe K line marked. *Right panel*: same for the second best solution at $z = 0.62$, consistent with the optical redshift.

# Appendix A: Redshift estimates of confirmed candidates

## A.1. Refinement of the XMM-Newton redshift estimate for $Q_z = 1$ cases

The redshift determination from *XMM-Newton* spectral analysis is uncertain for five clusters. There are several $\chi^2$ minima that cannot be distinguished at the 90% confidence level ($Q_z = 1$). As proposed by Planck Collaboration (2012), we estimated the $Y_X/Y_{500}$ and $F_X/Y_{500}$ ratios as a function of $z$ and compared them to expected values, to eliminate unphysical solutions.

Three possible redshifts were found for PLCK G352.1−24.0, 0.12, 0.4, and 0.77. The $Y_X/Y_{500}$ ratio method enables us to exclude the low redshift $z = 0.12$ solution. The $z = 0.4$ solution yields a $Y_X/Y_{500}$ ratio twice higher than expected, at the limit of the observed dispersion. Furthermore, we confirmed that there is no evidence of galaxy concentrations in the DSS red image at the precise *XMM-Newton* cluster location. We thus adopt the highest $z$ value, $z = 0.77$, confirming the cluster to be at high $z$.

The best fitting redshift for PLCK G239.9−40.0, $z = 0.74$, yields the $Y_X/Y_{500}$ ratio closest to expectation and is adopted in the further analysis. The lowest $z = 0.26$ solution is very unlikely, yielding a $Y_X/Y_{500}$ ratio twice as high as expected. The other possible solution is $z = 0.46$: there are some very faint objects in the DSS images at the *XMM-Newton* position, although whether those are galaxies is unclear.

In the case of PLCK G147.3−16.6, all three redshift solutions, 0.4, 0.62, and 1.03, yield a $Y_X/Y_{500}$ ratio within the observed dispersion. The best fitting value, $z = 1.03$, and the second best solution, $z = 0.62$, are consistent at the 90% confidence level, with $\chi^2$ values of 125.9 and 128.7 for 132 degree of freedom, respectively. The two models are shown in Fig. A.1. The optical measurement is described below (Sect. A.2).

The redshifts of the two components in PLCK G196.7−45.5 are uncertain. The $Y_X/Y_{500}$ and $F_X/Y_{500}$ ratio methods cannot be used for such double systems, since the individual SZ components are unresolved by *Planck*. Of the two solutions, $z = 0.57$ and $z = 0.87$ for PLCK G196.7−45.5A, the latter can be excluded: a clear concentration galaxies at the *XMM-Newton* location is visible in the DSS images, which thus cannot be at such high $z$ (see Sect. 2.2). For PLCK G196.7−45.5B we adopted the best fitting value, $z = 0.42$.
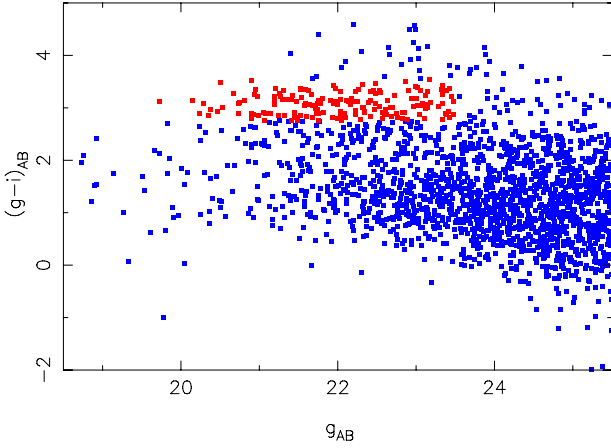
**Fig. A.2.** A $g - i$ vs. $g$ colour–magnitude diagram of non-stellar objects in the field of PLCK G147.3−16.6, observed with NOT/MOSCA. Galaxies plotted as red squares, in the region defined by $g - i = 3.15 \pm 0.40$ and $g < 23.5$, form the red sequence constituted by early-type galaxies in the cluster.

### A.2. Optical redshift estimate of PLCK G147.3–16.6

The optical data for PLCK G147.3−16.6 were taken using Director's Discretionary Time with DOLORES (Device Optimized for the LOw RESolution), a low resolution spectrograph and imager permanently installed at the TNG telescope (Telescopio Nazionale Galileo La Palma). The camera is equipped with a $2048 \times 2048$ pixel CCD covering a field of view of $8.'6 \times 8.'6$ (pixel scale of $0.''252$ per pixel). Exposure times of 3000 s in the $r$ and $i$ bands were split into 10 single exposures of 300 s each. Exposure times of 4000 s in the $z$ band were split into eight separate exposures. Taking advantage of the dither-offsets between single exposures, no separate sky images were required. The images were bias and flat field corrected using IRAF[6]. For astrometric calibration we used `astrometry.net`. The average seeing derived from the final images is $0.''84$, $0.''85$, and $0.''84$ in the $r$, $i$, and $z$-bands, respectively. In the final images, we reach signal-to-noise ratios (over the PSF area) of 11, 23, and 8 for unresolved sources of 24th magnitude. The colour composite image allows us to pre-identify the cluster members.

The cluster was also observed using the 2.56-m Nordic Optical Telescope with the MOSCA camera, a $2 \times 2$ mosaic of $2048 \times 2048$ pixel CCDs. This camera covers a total field of $7.'7 \times 7.'7$, and was used in $2 \times 2$ binned mode. This gives a pixel scale of $0.''217$ per binned pixel. Total exposure times of 900 s were split into 3 dithered exposures of 300 s in each of the SDSS $g$- and $i$-bands in photometric conditions. The telescope was pointed such that the two peaks of the X-ray emission from the cluster would fall in the centreof the mosaic CCD chip that has the best cosmetic quality (named "CCD7"). After standard basic reduction and image registration, the combined images had *FWHM* of $0.''79$ and $0.''65$ in the $g$ and $i$ bands, respectively. Photometric calibration was based on an ensemble of stars in a field located inside the SDSS footprint, observed at similar airmass immediately following the observations of PLCK G147.3−16.6. Stellar objects were removed from the object catalogues based on their location in a size-magnitude diagram. A strong clustering of galaxies with red $g - i$ colours was immediately detected around the position of the X-ray peaks. The colour-magnitude diagram in Fig. A.2 illustrates the red sequence formed by early-type galaxies at $g - i \simeq 3.15$ in this

cluster. Predicted $g - i$ colours of early-type galaxies as a function of redshift were calculated by convolving the EO template galaxy spectrum of Coleman et al. (1980) with the response curves of the SDSS $g$ and $i$ bandpasses. From this, a photometric redshift estimate of $z_{phot} = 0.64 \pm 0.03$ was derived.

The calibrated $g$- and $i$-band photometry from NOT was used to select suitable spectroscopic targets for Gemini North Telescope by choosing galaxies at $g - i \simeq 3.15$. The observations (Program GN-2011B-Q-41) were made with GMOS-N, with two exposures of 1800 s each. The program was in Band 2 service mode, with relaxed observing conditions: the seeing was $1.''7$ the first night and $0.''8$ the second night, with cirrus both nights. The observations were reduced with the standard Gemini IRAF package. We obtained redshift measurements for 13 objects. Among those, 10 have redshifts between 0.64 and 0.68, for a cluster redshift measurement of $0.66 \pm 0.05$. If we exclude two objects at $z = 0.68$, we obtain $z = 0.645 \pm 0.005$.

## Appendix B: Density maps of RASS bright and faint sources

In this appendix we describe the procedure used to calculate the density maps of RASS-BSC and FSC sources, and the associated probability of false association with a *Planck* cluster candidate. We use the catalogues downloaded from Vizier[7].

### B.1. Source density maps

To compute the source density maps, we use HEALPix[8] with a resolution of $N_{side} = 64$ (each pixel is 0.8 deg$^2$). The HEALPix function `ANG2PIX_RING` was used to compute the pixel number corresponding to the coordinates of the FSC/BSC sources.

At each pixel, we compute the source density by summing the number of sources in the pixels inside a disc of increasing radius until a threshold number of 10 sources is reached. The source density is then the number of sources found, $N_{src}$, divided by the number of pixels, $N_{pix}$, normalised by the area covered by one pixel:

$$\rho = \frac{N_{src}}{N_{pix}} \times (49\,152/4\pi) \times (\pi/180)^2 , \qquad (B.1)$$

where 49 152 is the total number of sky pixels for this resolution and $4\pi(180/\pi)^2 \approx 41\,000$ deg$^2$ is the total area of the sky. This gives the mean number of sources per square degree in each pixel.

The resulting source density maps are plotted in Figs. 10 and B.1. For the FSC density map, the mean source density per square degree ranges from 0.16 to 42.89. There is a clear correspondence between the source density and the depth of the RASS exposure, with regions of maximum source density lying in the regions of maximum RASS exposure at the ecliptic poles (Fig. 10). For the BSC density map, the mean source density per square degree ranges from 0.08 to 4.05, with a much less marked correspondence with the RASS exposure map (Fig. 10).

Figure B.2 shows the histogram of the number of pixels as a function of mean source density per square degree. We overplot on these histograms the mean ($\bar{\rho}$) and the median ($\rho_{1/2}$) value of the number of sources per square degree. We find $\bar{\rho} \approx \rho_{1/2} \sim 2$ sources deg$^{-2}$ for the FSC and $\bar{\rho} \approx \rho_{1/2} \sim 0.5$ sources deg$^{-2}$ for the BSC.

---

[6] IRAF: http://iraf.noao.edu

[7] http://vizier.u-strasbourg.fr
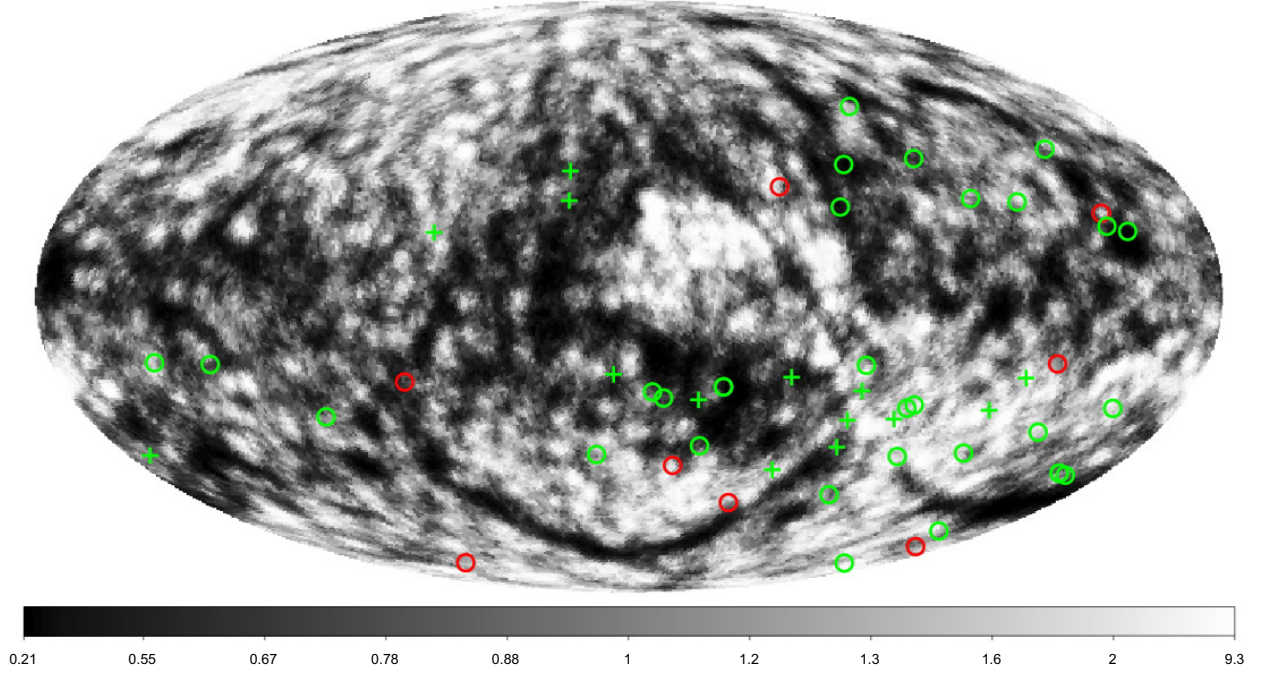[8] http://healpix.jpl.nasa.gov/

**Fig. B.1.** *XMM-Newton* validation results overplotted on density map of the RASS-Bright Source Catalogue (BSC). The source density map has been normalised by the median of the pixel density distribution. Confirmed candidates are plotted in green and false candidates are plotted in red. Pluses (+): good association with a BSC source. Circles (○): no association with a BSC source.
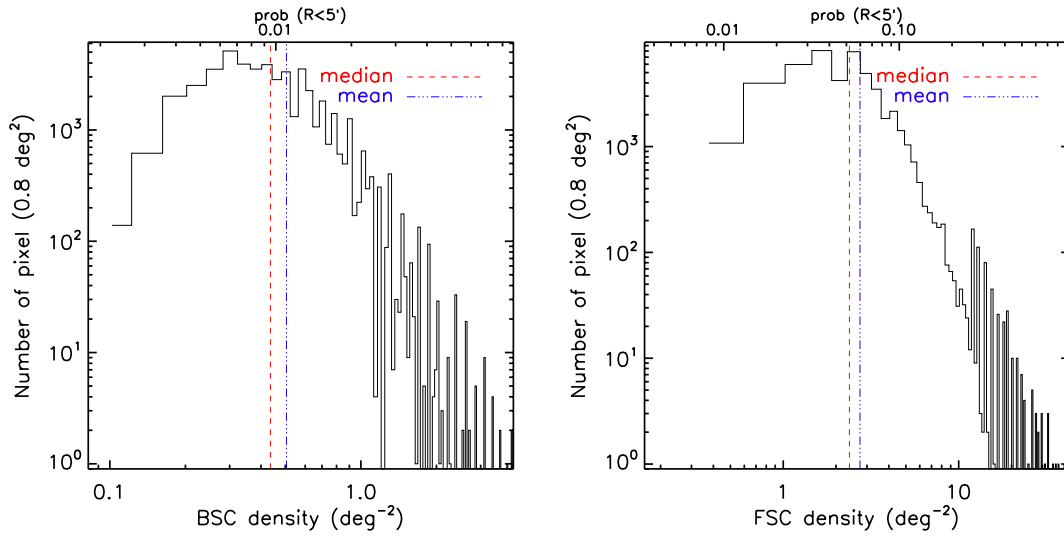


**Fig. B.2.** Histogram of the source density map of the RASS-BSC (*left panel*), and RASS-FSC (*right panel*), per square degree. The mean and median source density of each map are plotted in blue dot-dot-dot-dash and in red dashed lines, respectively. The upper *x*-axis shows the associated probability of association within 5′ (see text). The sources are drawn from the whole sky so the solid angle is $4\pi$ steradian.

### B.2. Probability of association within search radius $\mathcal{R}$

We can convert the local FSC/BSC source densities into probabilities of chance association of an SZ candidate with a FSC/BSC source. The probability of finding a cataloged FSC/BSC source within a search radius $\mathcal{R}$ of a *Planck* cluster candidate is the product of the FSC/BSC source density at the candidate location by the search area, $\mathcal{S}(\mathcal{R})$. This yields a mean probability of association of an SZ candidate with a B/FSC over the full sky of $\mathcal{S}(\mathcal{R} \leq 5') \times \bar{\rho} \sim 5\%$ for the FSC and 1% for the BSC. However, there is considerable variation depending on how well a given sky region is covered. In the most covered regions, the probability reaches nearly 95% of having an association within 5′ for the FSC and 9% for the BSC, while it decreases to 0.4% and 0.2% for the less covered regions for

**Table B.1.** Summary of the probability of chance association within 5′ for the RASS-FSC and the BSC.

| Catalogue | Min prob | Max prob | Mean prob | Median prob |
|---|---|---|---|---|
| FSC | 0.004 | 0.936 | 0.060 | 0.052 |
| BSC | 0.002 | 0.088 | 0.011 | 0.010 |

the FSC and BSC catalogues, respectively. We summarise these numbers in Table B.1.

### References

Angulo, R. E., Springel, V., White, S. D. M., et al. 2012, MNRAS, 426, 2046
Arnaud, M., Neumann, D. M., Aghanim, N., et al. 2001, A&A, 365, L80
Arnaud, M., Pratt, G. W., Piffaretti, R., et al. 2010, A&A, 517, A92
Bersanelli, M., Mandolesi, N., Butler, R. C., et al. 2010, A&A, 520, A4

Böhringer, H., Voges, W., Huchra, J. P., et al. 2000, ApJS, 129, 435
Böhringer, H., Schuecker, P., Guzzo, L., et al. 2004, A&A, 425, 367
Carlstrom, J. E., Ade, P. A. R., Aird, K. A., et al. 2011, PASP, 123, 568
Carvalho, P., Rocha, G., & Hobson, M. P. 2009, MNRAS, 393, 681
Carvalho, P., Rocha, G., Hobson, M. P., & Lasenby, A. 2012, MNRAS, 427, 1384
Coleman, G. D., Wu, C.-C., & Weedman, D. W. 1980, ApJS, 43, 393
Croston, J. H., Arnaud, M., Pointecouteau, E., & Pratt, G. W. 2006, A&A, 459, 1007
Croston, J. H., Pratt, G. W., Böhringer, H., et al. 2008, A&A, 487, 431
da Silva, A. C., Kay, S. T., Liddle, A. R., & Thomas, P. A. 2004, MNRAS, 348, 1401
Ebeling, H., Edge, A. C., Bohringer, H., et al. 1998, MNRAS, 301, 881
Ebeling, H., Edge, A. C., Allen, S. W., et al. 2000, MNRAS, 318, 333
Ebeling, H., Barrett, E., Donovan, D., et al. 2007, ApJ, 661, L33
Fassbender, R., Böhringer, H., Nastasi, A., et al. 2011, New J. Phys., 13, 125014
Kalberla, P. M. W., Burton, W. B., Hartmann, D., et al. 2005, A&A, 440, 775
Kravtsov, A. V., Vikhlinin, A., & Nagai, D. 2006, ApJ, 650, 128
Lamarre, J., Puget, J., Ade, P. A. R., et al. 2010, A&A, 520, A9
Mandolesi, N., Bersanelli, M., Butler, R. C., et al. 2010, A&A, 520, A3
Marriage, T. A., Baptiste Juin, J., Lin, Y., et al. 2011, ApJ, 731, 100
Melin, J., Bartlett, J. G., & Delabrouille, J. 2006, A&A, 459, 341
Mennella, A., Butler, R. C., Curto, A., et al. 2011, A&A, 536, A3
Piffaretti, R., Arnaud, M., Pratt, G. W., Pointecouteau, E., & Melin, J.-B. 2011, A&A, 534, A109
Planck Collaboration 2011a, A&A, 536, A8
Planck Collaboration 2011b, A&A, 536, A9
Planck Collaboration 2011c, A&A, 536, A11
Planck Collaboration 2011d, A&A, 536, A26
Planck Collaboration 2012, A&A, 543, A102
Planck HFI Core Team 2011, A&A, 536, A4
Pratt, G. W., Böhringer, H., Croston, J. H., et al. 2007, A&A, 461, 71
Pratt, G. W., Croston, J. H., Arnaud, M., & Böhringer, H. 2009, A&A, 498, 361
Pratt, G. W., Arnaud, M., Piffaretti, R., et al. 2010, A&A, 511, A85
Sunyaev, R. A. & Zeldovich, Y. B. 1972, Comm. Astrophys. Space Phys., 4, 173
Voges, W., Aschenbach, B., Boller, T., et al. 1999, A&A, 349, 389
Voges, W., Aschenbach, B., Boller, T., et al. 2000, VizieR Online Data Catalog, IX/029

[1] APC, AstroParticule et Cosmologie, Université Paris Diderot, CNRS/IN2P3, CEA/lrfu, Observatoire de Paris, Sorbonne Paris Cité, 10 rue Alice Domon et Léonie Duquet, 75205 Paris Cedex 13, France

[2] Aalto University Metsähovi Radio Observatory, Metsähovintie 114, 02540 Kylmälä, Finland

[3] Academy of Sciences of Tatarstan, Bauman Str., 20, 420111 Kazan, Republic of Tatarstan, Russia

[4] Agenzia Spaziale Italiana Science Data Center, c/o ESRIN, via Galileo Galilei, Frascati, Italy

[5] Agenzia Spaziale Italiana, Viale Liegi 26, Roma, Italy

[6] Astrophysics Group, Cavendish Laboratory, University of Cambridge, J J Thomson Avenue, Cambridge CB3 0HE, UK

[7] Atacama Large Millimeter/submillimeter Array, ALMA Santiago Central Offices, Alonso de Cordova 3107, Vitacura, Casilla 763 0355, Santiago, Chile

[8] CITA, University of Toronto, 60 St. George St., Toronto, ON M5S 3H8, Canada

[9] CNRS, IRAP, 9 Av. colonel Roche, BP 44346, 31028 Toulouse Cedex 4, France

[10] California Institute of Technology, Pasadena, California, USA

[11] Centre of Mathematics for Applications, University of Oslo, Blindern, Oslo, Norway

[12] Centro de Astrofísica, Universidade do Porto, Rua das Estrelas, 4150-762 Porto, Portugal

[13] Centro de Estudios de Física del Cosmos de Aragón (CEFCA), Plaza San Juan 1, planta 2, 44001 Teruel, Spain

[14] Computational Cosmology Center, Lawrence Berkeley National Laboratory, Berkeley, California, USA

[15] DSM/Irfu/SPP, CEA-Saclay, 91191 Gif-sur-Yvette Cedex, France

[16] DTU Space, National Space Institute, Juliane Mariesvej 30, Copenhagen, Denmark

[17] Département de Physique Théorique, Université de Genève, 24 Quai E. Ansermet, 1211 Genève 4, Switzerland

[18] Departamento de Física, Universidad de Oviedo, Avda. Calvo Sotelo s/n, Oviedo, Spain

[19] Department of Astronomy and Geodesy, Kazan Federal University, Kremlevskaya Str., 18, 420008 Kazan, Russia

[20] Department of Physics & Astronomy, University of British Columbia, 6224 Agricultural Road, Vancouver, British Columbia, Canada

[21] Department of Physics and Astronomy, Dana and David Dornsife College of Letter, Arts and Sciences, University of Southern California, Los Angeles, CA 90089, USA

[22] Department of Physics and Astronomy, University of Sussex, Brighton BN1 9QH, UK

[23] Department of Physics, Gustaf Hällströmin katu 2a, University of Helsinki, Helsinki, Finland

[24] Department of Physics, Princeton University, Princeton, New Jersey, USA

[25] Department of Physics, University of California, Berkeley, California, USA

[26] Department of Physics, University of California, One Shields Avenue, Davis, California, USA

[27] Department of Physics, University of California, Santa Barbara, California, USA

[28] Department of Physics, University of Illinois at Urbana-Champaign, 1110 West Green Street, Urbana, Illinois, USA

[29] Department of Statistics, Purdue University, 250 N. University Street, West Lafayette, Indiana, USA

[30] Dipartimento di Fisica e Astronomia G. Galilei, Università degli Studi di Padova, via Marzolo 8, 35131 Padova, Italy

[31] Dipartimento di Fisica, Università La Sapienza, P.le A. Moro 2, Roma, Italy

[32] Dipartimento di Fisica, Università degli Studi di Milano, via Celoria 16, Milano, Italy

[33] Dipartimento di Fisica, Università degli Studi di Trieste, via A. Valerio 2, Trieste, Italy

[34] Dipartimento di Fisica, Università di Ferrara, via Saragat 1, 44122 Ferrara, Italy

[35] Dipartimento di Fisica, Università di Roma Tor Vergata, via della Ricerca Scientifica 1, Roma, Italy

[36] Dipartimento di Matematica, Università di Roma Tor Vergata, via della Ricerca Scientifica 1, Roma, Italy

[37] Discovery Center, Niels Bohr Institute, Blegdamsvej 17, Copenhagen, Denmark

[38] Dpto. Astrofísica, Universidad de La Laguna (ULL), 38206 La Laguna, Tenerife, Spain

[39] European Southern Observatory, ESO Vitacura, Alonso de Cordova 3107, Vitacura, Casilla 19001, Santiago, Chile

[40] European Space Agency, ESAC, Camino bajo del Castillo s/n, Urbanización Villafranca del Castillo, Villanueva de la Cañada, Madrid, Spain

[41] European Space Agency, ESAC, Planck Science Office, Camino bajo del Castillo s/n, Urbanización Villafranca del Castillo, Villanueva de la Cañada, Madrid, Spain

[42] European Space Agency, ESTEC, Keplerlaan 1, 2201 AZ Noordwijk, The Netherlands

[43] GEPI, Observatoire de Paris, Section de Meudon, 5 place J. Janssen, 92195 Meudon Cedex, France

[44] Helsinki Institute of Physics, Gustaf Hällströmin katu 2, University of Helsinki, Helsinki, Finland

[45] INAF – Osservatorio Astronomico di Padova, Vicolo dell'Osservatorio 5, Padova, Italy

[46] INAF – Osservatorio Astronomico di Roma, via di Frascati 33, Monte Porzio Catone, Italy

[47] INAF – Osservatorio Astronomico di Trieste, via G.B. Tiepolo 11, Trieste, Italy

[48] INAF Istituto di Radioastronomia, via P. Gobetti 101, 40129 Bologna, Italy

[49] INAF/IASF Bologna, via Gobetti 101, Bologna, Italy

[50] INAF/IASF Milano, via E. Bassini 15, Milano, Italy

[51] INFN, Sezione di Roma 1, Università di Roma Sapienza, Piazzale Aldo Moro 2, 00185 Roma, Italy

[52] INRIA, Laboratoire de Recherche en Informatique, Université Paris-Sud 11, Bâtiment 490, 91405 Orsay Cedex, France

[53] IPAG: Institut de Planétologie et d'Astrophysique de Grenoble, Université Joseph Fourier, Grenoble 1 / CNRS-INSU, UMR 5274, 38041 Grenoble, France

[54] IUCAA, Post Bag 4, Ganeshkhind, Pune University Campus, 411 007 Pune, India

[55] Imperial College London, Astrophysics group, Blackett Laboratory, Prince Consort Road, London SW7 2AZ, UK

[56] Infrared Processing and Analysis Center, California Institute of Technology, Pasadena, CA 91125, USA

[57] Institut Néel, CNRS, Université Joseph Fourier Grenoble I, 25 rue des Martyrs, Grenoble, France

[58] Institut Universitaire de France, 103 Bd Saint-Michel, 75005 Paris, France

[59] Institut d'Astrophysique Spatiale, CNRS UMR8617 Université Paris-Sud 11, Bâtiment 121, Orsay, France

[60] Institut d'Astrophysique de Paris, CNRS UMR7095, 98bis boulevard Arago, 75014 Paris, France

[61] Institute for Space Sciences, Bucharest-Magurale, Romania

[62] Institute of Astro and Particle Physics, Technikerstrasse 25/8, University of Innsbruck, 6020 Innsbruck, Austria

[63] Institute of Astronomy and Astrophysics, Academia Sinica, Taipei, Taiwan

[64] Institute of Astronomy, University of Cambridge, Madingley Road, Cambridge CB3 0HA, UK

[65] Institute of Theoretical Astrophysics, University of Oslo, Blindern, Oslo, Norway

[66] Instituto de Astrofísica de Canarias, C/Vía Láctea s/n, La Laguna, Tenerife, Spain

[67] Instituto de Física de Cantabria (CSIC-Universidad de Cantabria), Avda. de los Castros s/n, Santander, Spain

[68] Istituto di Fisica del Plasma, CNR-ENEA-EURATOM Association, via R. Cozzi 53, Milano, Italy

[69] Jet Propulsion Laboratory, California Institute of Technology, 4800 Oak Grove Drive, Pasadena, California, USA

[70] Jodrell Bank Centre for Astrophysics, Alan Turing Building, School of Physics and Astronomy, The University of Manchester, Oxford Road, Manchester M13 9PL, UK

[71] Kavli Institute for Cosmology Cambridge, Madingley Road, Cambridge CB3 0HA, UK

[72] LAL, Université Paris-Sud, CNRS/IN2P3, Orsay, France

[73] LERMA, CNRS, Observatoire de Paris, 61 avenue de l'Observatoire, Paris, France

[74] Laboratoire AIM, IRFU/Service d'Astrophysique – CEA/DSM – CNRS – Université Paris Diderot, Bât. 709, CEA-Saclay, 91191 Gif-sur-Yvette Cedex, France
e-mail: `jessica.democles@cea.fr`

[75] Laboratoire de Physique Subatomique et de Cosmologie, Université Joseph Fourier Grenoble I, CNRS/IN2P3, Institut National Polytechnique de Grenoble, 53 rue des Martyrs, 38026 Grenoble Cedex, France

[76] Laboratoire de Physique Théorique, Université Paris-Sud 11 & CNRS, Bâtiment 210, 91405 Orsay, France

[77] Lawrence Berkeley National Laboratory, Berkeley, California, USA

[78] Max-Planck-Institut für Astrophysik, Karl-Schwarzschild-Str. 1, 85741 Garching, Germany

[79] Max-Planck-Institut für Extraterrestrische Physik, Giessenbachstraße, 85748 Garching, Germany

[80] Niels Bohr Institute, Blegdamsvej 17, Copenhagen, Denmark

[81] Observational Cosmology, Mail Stop 367-17, California Institute of Technology, Pasadena, CA, 91125, USA

[82] Optical Science Laboratory, University College London, Gower Street, London, UK

[83] SISSA, Astrophysics Sector, via Bonomea 265, 34136 Trieste, Italy

[84] SUPA, Institute for Astronomy, University of Edinburgh, Royal Observatory, Blackford Hill, Edinburgh EH9 3HJ, UK

[85] School of Physics and Astronomy, Cardiff University, Queens Buildings, The Parade, Cardiff CF24 3AA, UK

[86] Space Research Institute (IKI), Russian Academy of Sciences, Profsoyuznaya Str, 84/32, 117997 Moscow, Russia

[87] Space Sciences Laboratory, University of California, Berkeley, California, USA

[88] Stanford University, Dept of Physics, Varian Physics Bldg, 382 via Pueblo Mall, Stanford, California, USA

[89] UPMC Univ. Paris 6, UMR7095, 98bis boulevard Arago, 75014 Paris, France

[90] Université Denis Diderot (Paris 7), 75205 Paris Cedex 13, France

[91] Université de Toulouse, UPS-OMP, IRAP, 31028 Toulouse Cedex 4, France

[92] University Observatory, Ludwig Maximilian University of Munich, Scheinerstrasse 1, 81679 Munich, Germany

[93] University of Granada, Departamento de Física Teórica y del Cosmos, Facultad de Ciencias, Granada, Spain

[94] University of Miami, Knight Physics Building, 1320 Campo Sano Dr., Coral Gables, Florida, USA

[95] Warsaw University Observatory, Aleje Ujazdowskie 4, 00-478 Warszawa, Poland